nature communications

Article

https://doi.org/10.1038/s41467-026-71409-9

VPS26A retromer complex and SNX27 mediate stress-induced Golgi bypass of membrane proteins

Received: 26 May 2025

Accepted: 18 March 2026

Published online: 06 April 2026

Check for updates

Ye Jin Kim[1,7], Chaeyoung Lee[1,7], Soo Kyung Seo[1], Jae Won Roh[1], Hye Ryung Lee[1], Su Jin Hwang[2], Nienping Chang[3], Hee Seong Choi[3], Dong Hoon Shin[1], Hui Kwon Kim[4], Han Sang Kim[5], Hyun-Soo Cho[3], Jae Myun Lee[2], Heon Yung Gee[1], Min Goo Lee[1,6] ✉ & Shin Hye Noh[1,6] ✉

Many proteins can reach the cell surface through a Golgi-independent unconventional protein secretion (UPS) pathway, particularly under cellular stress conditions. However, the molecular mechanisms that mediate UPS remain largely elusive. In this study, VPS26A-containing retromer complex, along with the sorting nexin SNX27, is identified as a regulator of UPS of transmembrane proteins, including the trafficking-deficient ΔF508 mutant CFTR, which causes cystic fibrosis, and the SARS-CoV-2 spike protein, associated with COVID-19. A targeted CRISPR knockout screen identified VPS26A as a key contributor in the UPS of ΔF508-CFTR. Subsequent molecular analyses revealed that SNX27 recruits ΔF508-CFTR to the VPS26A-VPS35-VPS29 retromer complex, facilitating its transport to the cell surface under UPS-inducing conditions. Additionally, VPS26A and SNX27 are necessary for UPS of the spike protein, enabling the formation of intact SARS-CoV-2 virions. These findings suggest that the retromer complex and SNX27, known for their roles in recycling endosomes, mediate previously unrecognized functions in the UPS of transmembrane proteins.

Cellular proteins are transported to appropriate sites after synthesis to perform their specific functions within subcellular microdomains. It is well established that most secretory and transmembrane proteins are transported via the endoplasmic reticulum (ER)-to-Golgi pathway[1,2]. However, increasing evidence suggests that proteins can move through alternative pathways in addition to the typical protein transport pathway[3,4]. While much remains to be uncovered about these alternative pathways, researchers have identified a number of cytosolic and membrane proteins that reach the plasma membrane via Golgi-independent routes[5,6], collectively known as unconventional protein secretion (UPS) pathways. UPS can be categorized into three or four subtypes, one of which involves the Golgi-bypass of transmembrane proteins. A well-known example of this is the Golgi-independent transport of the cystic fibrosis transmembrane conductance regulator (CFTR)[7].

CFTR is an anion channel that facilitates the transport of chloride and bicarbonate anions in epithelial cells[8]. Defective CFTR genes have been linked to the development of chronic genetic diseases such as

[1]Department of Pharmacology, Brain Korea 21 Project for Medical Science, Woo Choo Lee Institute for Precision Drug Development, Yonsei University College of Medicine, Seoul, Republic of Korea. [2]Department of Microbiology and Immunology, Institute for Immunology and Immunological Diseases, Brain Korea 21 Project for Medical Science, Yonsei University College of Medicine, Seoul, Republic of Korea. [3]Department of Systems Biology and Division of Life Sciences, Yonsei University, Seoul, Republic of Korea. [4]Department of Integrative Biotechnology, Sungkyunkwan University, Suwon, Republic of Korea. [5]Division of Medical Oncology, Department of Internal Medicine, Yonsei Cancer Center, Yonsei University College of Medicine, Seoul, Republic of Korea. [6]Severance Biomedical Science Institute, Yonsei University College of Medicine, Seoul, Republic of Korea. [7]These authors contributed equally: Ye Jin Kim, Chaeyoung Lee. ✉e-mail: mlee@yuhs.ac; alley282@yuhs.ac

cystic fibrosis and pancreatitis. Among patients with cystic fibrosis, the most prevalent mutation is ΔF508-CFTR, where phenylalanine at position 508 of the CFTR protein is deleted. The synthesis of the ΔF508-CFTR mutant protein leads to structural and folding abnormalities, which subsequently cause a trafficking deficiency in ER exit and degradation through the ER-associated degradation (ERAD) mechanism[9–11]. Consequently, in patients with the ΔF508-CFTR mutation, there is an absence of CFTR protein at the cell membrane, which impairs anion transport and ultimately leads to disease development. Previous studies have shown that, under certain circumstances, such as the induction of ER stress or blockade of ER-to-Golgi transport, the ER core-glycosylated form of CFTR, including the ΔF508 mutant, can be transported to the cell membrane via the UPS pathway, bypassing the Golgi apparatus[12–15]. Notably, the unconventionally transported ΔF508-CFTR retains a certain level of functional activity at the cell surface[12–15], suggesting that activation of the UPS pathway has the potential to treat the disease.

Severe acute respiratory syndrome coronavirus 2 (SARS-CoV-2), the etiologic agent of COVID-19, has a spike protein in its envelope that plays a critical role in the infection of host cells[16]. It has been suggested that UPS pathways are employed in the viral egress process and also the trafficking of spike proteins throughout SARS-CoV-2 infection. For example, the Golgi apparatus becomes fragmented during SARS-CoV-2 infection[17,18], indicating a potential for the activation of Golgi-independent pathways. Furthermore, SARS-CoV-2 uses an endo-lysosomal system for egress, rather than the conventional secretory pathway[19].

Despite considerable progress made recently, the molecular mechanisms of UPS remain largely elusive[6,20]. For example, several studies have proposed a link between recycling endosomes and UPS or secretory autophagy, a non-degradative form of autophagy that shares many common aspects with, or is regarded as a form of, UPS[14,21]. However, the key regulatory factors and molecular machinery involved in the interplay between endosomes and UPS or secretory autophagy remain unclear. In this study, we performed a CRISPR knockout (KO) screen using a custom single-guide RNA (sgRNA) library to identify molecules essential for the regulation of the UPS in ΔF508-CFTR. This initial analysis identified VPS26A, a component of the retromer complex, as exerting a strong regulatory influence on CFTR UPS. Subsequent investigation revealed that the trimeric VPS26A-VPS35-VPS29 retromer complex, together with the PDZ (postsynaptic density 95/discs large/zonula occludens-1) domain-containing sorting nexin 27 (SNX27), known to direct the retromer to early and recycling endosomes[22], participates in the Golgi-independent cell surface trafficking of ΔF508-CFTR and SARS-CoV-2 spike protein, particularly under certain cellular stress conditions. These findings broaden our understanding of how endosomal sorting machinery, classically linked to recycling and retrograde transport, can be repurposed to facilitate the stress-induced Golgi-independent trafficking.

Results

The VPS26A retromer complex participates in the UPS of ΔF508-CFTR

We initially performed genetic screening using the CRISPR KO system to identify factors involved in the UPS of the transmembrane protein CFTR (Fig. 1a). Genes involved in vesicular transport, autophagy, and ER stress were selected for CRISPR/Cas9 KO screening in Cas9-expressing HeLa cells. A total of 9072 single-guide (sg) RNAs targeting 1082 genes were designed, as described in the "Materials and Methods" section (Supplementary Fig. 1 and Supplementary Data 1 and 2). To monitor cell-surface expression of CFTR, cells were transfected with plasmids encoding extracellular HA-tagged CFTR and stained with phycoerythrin (PE)-conjugated anti-HA antibodies. Cells were then analyzed and sorted by fluorescence-activated cell sorting (FACS) (Fig. 1a, b). To establish a gating threshold for PE-positive cells, we first measured PE intensity in cells expressing wild-type CFTR, which efficiently traffics to the plasma membrane via the conventional secretory pathway (Fig. 1b left). In contrast, cells expressing ΔF508-CFTR alone showed minimal PE signal (Fig. 1b middle), confirming that background surface expression is negligible without rescue. Based on this comparison, we defined a PE intensity threshold (P4 gate) to identify cells with significant CFTR surface expression. To induce UPS activation, cells were co-expressed with the dominant-inhibitory form of ADP-ribosylation factor 1 (ARF1-Q71L, Fig. 1b right), which blocks the conventional ER-to-Golgi transport pathway and thereby activates alternative secretion pathways[23].

Next-generation sequencing (NGS) was performed on PE-positive (rescued) and total populations of ΔF508-CFTR-expressing cells co-transfected with ARF1-Q71L to identify genes regulating UPS. Analysis of sgRNA sequences using the MAGeCK algorithm identified VPS26A, a core component of the retromer complex, as the top-ranked factor required for CFTR UPS (Fig. 1c and Supplementary Data 3). The involvement of VPS26A in ΔF508-CFTR UPS was also verified via cell-surface biotinylation assay, in which knockdown of VPS26A greatly reduced the ARF1-Q71L-induced cell-surface expression of ΔF508-CFTR (Fig. 1d, e). In addition to ARF1-Q71L, the blockade of ER-to-Golgi transport using the dominant-inhibitory form of the secretion-associated and Ras-related protein 1 (SAR1-T39N), along with the overexpression of the *cis*-Golgi target SNARE protein syntaxin 5 (STX5), has been shown to induce UPS of the trafficking-deficient ΔF508-CFTR via the activation of an ER stress-associated mechanism[12,13]. As shown in Fig. 1f–i, the knockdown of VPS26A also greatly reduced ΔF508-CFTR UPS induced by SAR1-T39N and STX5 overexpression, indicating a common requirement for VPS26A under ER stress-associated conditions.

Retromer mediates the sorting of cargo proteins within endosomes, generally directing them either to be transported back to the trans-Golgi network or recycled to the plasma membrane in animal cells, rather than being targeted for degradation in lysosomes[22,24]. The core retromer complex is composed of three vacuolar protein sorting (VPS) proteins in mammalian cells: VPS26, VPS29, and VPS35[22,24]. We thus examined whether VPS29 and VPS35 are involved in the UPS of ΔF508-CFTR. Notably, the silencing of both VPS29 and VPS35 resulted in inhibition of the UPS of ΔF508-CFTR induced by ARF1-Q71L, indicating that a whole retromer complex is necessary for the ER stress-associated UPS (Fig. 2a–d). Since VPS26B, like VPS26A, is a known component of a retromer complex[25], we also investigated its potential involvement in CFTR UPS. As shown in Supplementary Fig. 2, silencing of VPS26B reduced the surface level of ΔF508-CFTR (surface biotinylation; Supplementary Fig. 2a, b); however, it also significantly decreased the total cellular level of ΔF508-CFTR (cell lysate; Supplementary Fig. 2a, c), which hampers the precise determination of trafficking effects. We therefore conducted all subsequent experiments using VPS26A to focus on trafficking events without affecting protein stability.

Next, we examined whether these proteins are also involved in the conventional Golgi-mediated trafficking of wild-type CFTR. As CFTR is an N-glycosylated protein, its core glycosylation occurs in the ER, while complex glycosylation takes place in the Golgi apparatus. The complex-glycosylated form, commonly referred to as band C, has a higher molecular weight than the core-glycosylated form, referred to as band B. Wild-type CFTR primarily appears as band C in immunoblots, as it passes through the Golgi, whereas the ΔF508-CFTR variant appears as band B because it is retained in the ER[12]. Interestingly, knockdowns of VPS26A, VPS29, and VPS35 did not affect the conventional Golgi-mediated trafficking of the band C form of wild-type CFTR to the cell surface (Fig. 2e–j). The blockade of ER-to-Golgi transport by ARF1-Q71L also induced the UPS of wild-type CFTR, resulting in the appearance of the band B form of CFTR on the cell surface due to trafficking via a Golgi-bypass route. Notably, knockdowns of VPS26A,

https://doi.org/10.1038/s41467-026-71409-9

VPS29, and VPS35 significantly inhibited the UPS of ER form (band B) of wild-type CFTR (Fig. 2e–j). These findings indicate that the retromer complex is more crucial for the Golgi-independent UPS of CFTR rather than conventional Golgi-mediated transport.

SNX27 recruits CFTR to the retromer complex through PDZ-based interaction

The mammalian retromer complex functions as a coat complex that regulates intracellular trafficking in general by interacting with sorting nexins (SNXs), which serve as adaptor proteins that link retromer to specific cargo or membrane domains[24,26–28]. We then examined whether SNXs are potentially involved in the regulation of CFTR UPS in conjunction with the retromer complex. We focused primarily on SNX27, which has been shown to recruit transmembrane protein cargos containing a PDZ-binding motif at their C-terminus, such as the β2-adrenergic receptor[29], the glucose transporter GLUT1[30], and the AMPA receptor subunit GluA1[31]. SNX27 is composed of PDZ, PX (phosphoinositide-binding Phox homology), and FERM (4.1/ezrin/radixin/moesin) domains. Notably, structural analyses have revealed that the PDZ domain of SNX27 plays a critical role in recruiting cargo to the retromer complex by simultaneously binding the PDZ-binding motifs of membrane proteins, while an exposed β-hairpin within the SNX27 PDZ domain engages a groove in VPS26[32]. Because CFTR is also a plasma membrane protein bearing a C-terminal PDZ-binding motif[33,34], we prioritized SNX27 as a mechanistically plausible adaptor for CFTR UPS. As shown in Fig. 3a, b, silencing of SNX27 resulted in a strong reduction

https://doi.org/10.1038/s41467-026-71409-9

Fig. 1 | VPS26A is involved in the UPS of ΔF508-CFTR. a Schematic representation of the CRISPR-Cas9 knockout screening workflow. A customized CRISPR/Cas9 knockout library containing 9072 sgRNAs was packaged into lentiviral particles and transduced into Cas9-overexpressing HeLa cells (HeLa-Cas9) at a low multiplicity of infection (MOI). Transduced cells were selected with puromycin for 6 days before transfection with both HA-tagged ΔF508-CFTR and ARF1-Q71L plasmids. The following day, cells were stained with a PE-conjugated HA antibody, and PE-positive cells were sorted by flow cytometry. Genomic DNA was extracted, and sgRNA sequences were amplified by PCR and analyzed. **b** Flow cytometry gating strategy for detecting cell-surface CFTR. Cells expressing wild-type CFTR, ΔF508-CFTR, or ΔF508-CFTR with ARF1-Q71L were analyzed for PE fluorescence after anti-HA staining. The P4 gate was defined based on the PE intensity distribution of WT-CFTR and used as a threshold for surface expression (left). ΔF508-CFTR alone showed negligible PE signal, confirming the specificity of gating (middle). Cells co-expressing ARF1-Q71L exhibited rescue of ΔF508-CFTR to the cell surface (right, red rectangle) and were sorted as the PE-positive population. **c** MAGeCK-based CRISPR screen plot comparing gene-level enrichment in PE-positive (rescued) versus total unsorted cells, both expressing ΔF508-CFTR and ARF1-Q71L. Genes whose knockout reduced surface CFTR rescue are shown on the left. Statistical analysis was performed using the MAGeCK test with directional negative-selection analysis. **d**–**i** Effects of VPS26A silencing on ΔF508-CFTR UPS. HEK293 cells were transfected with either control siRNA or VPS26A siRNA (50 nM, 48 h). After 24 h, cells were further transfected with plasmids encoding ΔF508-CFTR. In some conditions, **d** ARF1-Q71L, **f** SAR1-T39N, or **h** Syntaxin5 was co-transfected to induce ER stress (24 h). Cell surface biotinylation assays were performed to assess CFTR trafficking. VPS26A knockdown efficiency was confirmed with immunoblotting of cell lysates. Representative immunoblots and quantification from three independent experiments are shown ($n = 3$). Bar graphs show mean ± SEM. Statistical analyses for (**e**, **g**, and **i**) were performed using one-way ANOVA followed by Tukey's multiple comparison test. *b*, core-glycosylated CFTR.

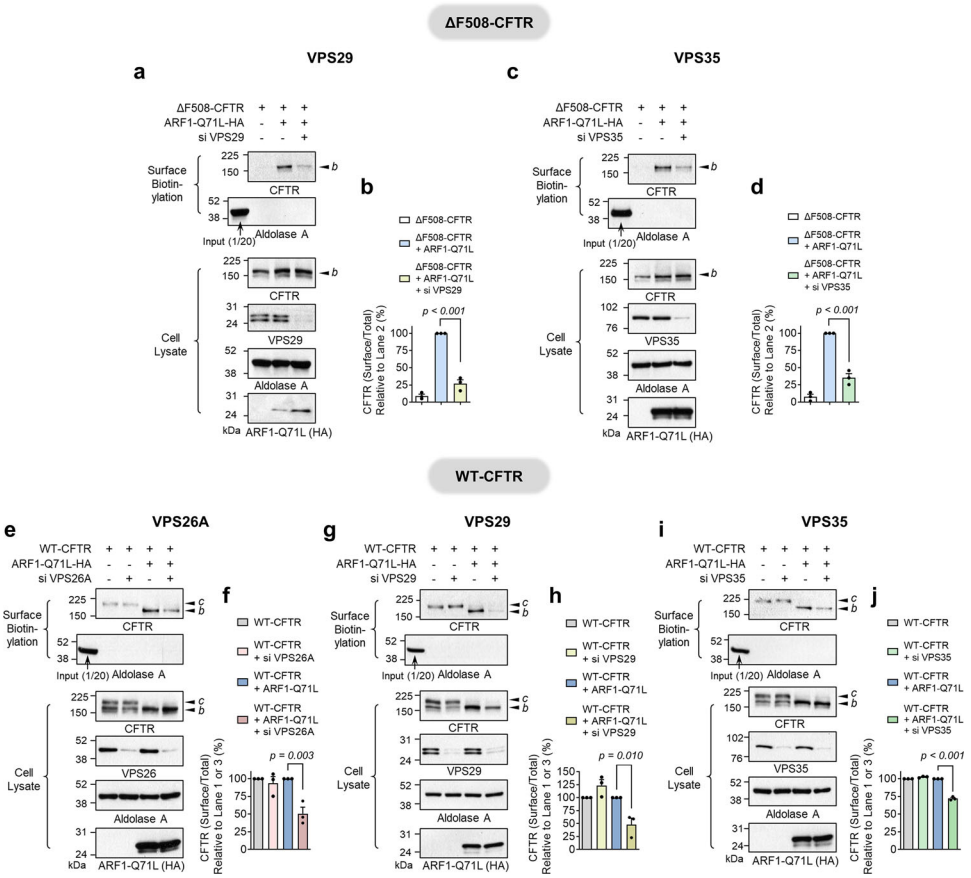

Fig. 2 | The VPS26-VPS29-VPS35 retromer complex participates in the UPS of CFTR. a–**d** Effects of VPS29 and VPS35 silencing on the unconventional secretion (UPS) of ΔF508-CFTR. HEK293 cells were transfected with control siRNA or siRNAs targeting VPS29 or VPS35 (50 nM, 48 h). After 24 h, cells were further transfected with ΔF508-CFTR plasmids, with or without ARF1-Q71L co-transfection to induce ER stress (24 h). CFTR trafficking was assessed using a cell surface biotinylation assay. The core-glycosylated form of CFTR (band b) is indicated. Representative immunoblots are shown in (**a** and **c**), with quantification from three independent experiments shown in (**b** and **d**) ($n = 3$). **e**–**j** Effects of VPS26A, VPS29, and VPS35 silencing on the conventional secretion of WT-CFTR. HEK293 cells were transfected with control siRNA or siRNAs targeting VPS26A, VPS29, and VPS35 (50 nM, 48 h), followed by WT-CFTR plasmid transfection (24 h). In some conditions, ARF1-Q71L was co-transfected to induce ER stress. The complex-glycosylated form of CFTR (band c) is indicated. Representative immunoblots are shown in (**e**, **g**, and **i**), with quantification from three independent experiments shown in (**f**, **h**, and **j**) ($n = 3$), respectively. Bar graphs represent mean ± SEM. All statistical analyses shown in this figure were performed using one-way ANOVA followed by Tukey's multiple comparison test. *b*, core-glycosylated CFTR; *c*, complex-glycosylated CFTR.

in the ΔF508-CFTR UPS induced by ARF1-Q71L. Like the retromer components, silencing of the SNX27 gene reduced UPS of wild-type CFTR (band B) but not its conventional trafficking (band C) (Fig. 3c, d).

We next investigated whether SNX27 functions as a cargo receptor for CFTR by assessing its ability to bind to CFTR using a co-immunoprecipitation (co-IP) assay. The co-IP results indicate that SNX27 associates with ΔF508-CFTR (Fig. 3e, f). It is noteworthy that the SNX27-CFTR association was augmented when UPS was induced by ARF1-Q71L, implying that SNX27 may play a prominent role during the UPS process. Subsequent immunocytochemistry experiments revealed that SNX27 co-localizes with ΔF508-CFTR during UPS (Fig. 3g, h), which is in line with the co-IP results. Based on these findings, which

https://doi.org/10.1038/s41467-026-71409-9

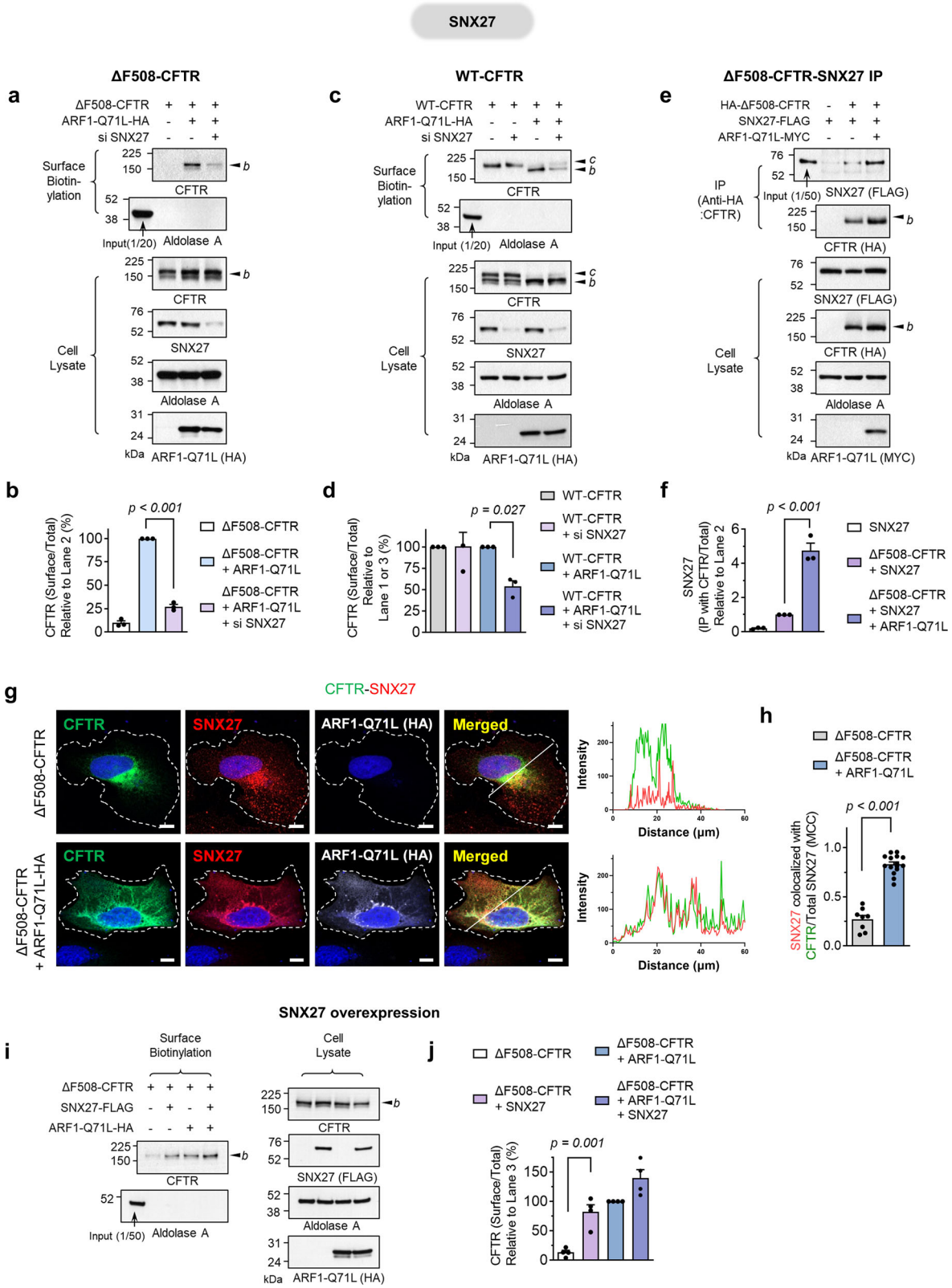

demonstrate the potential role of SNX27 in CFTR UPS, we examined the impact of SNX27 upregulation on the induction of ΔF508-CFTR UPS. Notably, SNX27 overexpression partially restored mutant CFTR expression at the plasma membrane and further enhanced ARF1-mediated rescue of its surface localization (Fig. 3i, j), suggesting that SNX27 promotes vesicular membrane trafficking of ΔF508-CFTR via a route bypassing the Golgi.

We next tested whether SNX27 engages CFTR in a PDZ-dependent manner and thereby couples CFTR to the retromer complex via VPS26. In the co-IP experiments shown in Fig. 4a, b, the deletion of four amino acids from the CFTR C-terminus (CFTR-ΔC), which disrupted its PDZ-binding motif, prevented its interaction with SNX27. This strongly indicates that the CFTR-SNX27 association is mediated by a PDZ-based interaction. To further validate this notion, we fragmented and

Fig. 3 | SNX27 physically interacts with CFTR and regulates its UPS. a–d Effects of SNX27 silencing on CFTR trafficking. HEK293 cells were transfected with control siRNA or SNX27 siRNA (50 nM, 48 h), followed by ΔF508-CFTR or WT-CFTR plasmid transfection (24 h). In some conditions, ARF1-Q71L was co-transfected to induce ER stress. Core-glycosylated (band b) and complex-glycosylated (band c) CFTR forms are indicated. Representative immunoblots are shown in (**a** and **c**), with quantification from three independent experiments shown in (**b** and **d**) ($n = 3$). **e**, **f** SNX27 interacts with ΔF508-CFTR. Immunoprecipitation was performed using anti-HA antibody-conjugated beads in HEK293 cells transfected with FLAG-tagged SNX27 alone or co-transfected with HA-ΔF508-CFTR. ARF1-Q71L was co-expressed in some conditions to induce unconventional protein secretion. Representative blots and quantification from three independent experiments are shown in (**e** and **f**) ($n = 3$), respectively. Bar graphs show mean ± SEM. Statistical analyses for (**b**, **d**, and **f**) were performed using one-way ANOVA followed by Tukey's multiple comparison test. *b*, core-glycosylated CFTR; *c*, complex-glycosylated CFTR. **g**, **h** Immunofluorescence analysis of SNX27 and ΔF508-CFTR. HeLa cells were transfected with ΔF508-CFTR, with or without ARF1-Q71L co-transfection (24 h). ΔF508-CFTR was stained with anti-CFTR ACL006 antibodies (green, Alexa Fluor 488), endogenous SNX27 with anti-SNX27 antibodies (red, Alexa Fluor 568), and ARF1-Q71L with anti-HA antibodies (pseudo-white, Alexa Fluor 680). The nucleus was counterstained with DAPI (blue color). Representative images are shown in (**g**), and Manders' co-localization coefficient (MCC) analysis is summarized in (**h**) ($n = 8$ cells for ΔF508-CFTR and $n = 15$ cells for ΔF508-CFTR + ARF1-Q71L, from 3 independent experiments). The white dotted line indicates the regions selected for quantification, and the white straight line in the merged images marks the line used for line-scan analysis with the corresponding intensity profiles shown on the right. Bar graphs show mean ± SEM. Statistical analysis for (**h**) was performed using a two-tailed Student's *t*-test. Additional representative images are available in Supplementary Fig. 11. Scale bar: 10 μm. **i**, **j** Effects of SNX27 overexpression on ΔF508-CFTR surface expression. HEK293 cells were transfected with ΔF508-CFTR, SNX27, or ARF1-Q71L (36 h), followed by surface biotinylation and immunoblotting. Representative blots and quantification from three independent experiments are shown in (**i** and **j**) ($n = 4$), respectively. Bar graphs show mean ± SEM. Statistical analysis for (**j**) was performed using one-way ANOVA followed by Tukey's multiple comparison test. *b*, core-glycosylated CFTR.

purified each of the three domains of SNX27 (PDZ, PX, and C-terminal FERM) as illustrated in Fig. 4c and then performed pull-down assays using a GST-tagged peptide containing the C-terminal 30 amino acids of CFTR (CFTR-Ct30). The results evidently demonstrate that the PDZ domain of SNX27, and not its other domains, binds to CFTR-Ct30 (Fig. 4d).

Subsequently, we investigated the overall physical interactions of SNX27, VPS26A, and CFTR. In co-IP experiments, VPS26A and SNX27 were found to interact with each other (Fig. 4e, f), consistent with previous reports[30,32]. Notably, this interaction was significantly enhanced by UPS induction via ARF1-Q71L and the co-expression of the cargo protein CFTR, resulting in a tenfold increase in SNX27-VPS26A interaction when ARF1-Q71L and CFTR were co-expressed (Fig. 4e, f). Additionally, the interaction between SNX27 PDZ and VPS26A increased proportionally with the amount of CFTR-Ct30 (Fig. 4g, h). Furthermore, in semi-in vivo pull-down assays using purified SNX27 PDZ and CFTR-Ct30, VPS26A failed to interact with the CFTR C-terminus in the absence of the SNX27 PDZ domain (Fig. 4i). These findings indicate that SNX27 is essential for the association of the retromer complex with the UPS cargo protein CFTR.

To quantitatively assess the SNX27-VPS26A interaction, we performed surface plasmon resonance (SPR) analysis using immobilized VPS26A and soluble SNX27-PDZ, either alone or pre-incubated with CFTR-Ct30. Consistent with our co-IP and pull-down results, the presence of CFTR markedly increased the affinity of SNX27-PDZ for VPS26A. SNX27-PDZ alone exhibited a dissociation constant (K_D) of approximately 51.4 μM, whereas the SNX27-PDZ–CFTR-Ct30 complex bound VPS26A with substantially higher affinity ($K_D = 3.8$ μM; Fig. 4j and Supplementary Fig. 3). These findings provide additional biophysical evidence that CFTR binding strengthens the SNX27-VPS26A interaction.

We then examined whether the VPS26A- and SNX27-mediated route represents a common pathway for the UPS of CFTR. It has been shown that induction of ER stress by thapsigargin treatment triggers the UPS of ΔF508-CFTR[12]. Notably, knockdowns of VPS26A and SNX27 significantly reduced thapsigargin-induced ΔF508-CFTR UPS (Fig. 5a, b), indicating that VPS26A and SNX27 participate in the UPS pathway under multiple ER stress conditions.

GRASPs, also known as GORASPs, are involved in the UPS of many cargo molecules across a wide variety of organisms[4,35]. Having identified SNX27 as a PDZ-dependent adaptor for CFTR UPS, and given that mammalian GRASP55 (GORASP2) is a well-established UPS modulator and a PDZ-containing protein[12,20], we further investigated how these two adaptors function within the UPS pathway. Combined knockdown of SNX27 and GRASP55 further decreased ARF1-Q71L-induced UPS of ΔF508-CFTR compared with either single knockdown (Fig. 5c, d), indicating that the two PDZ adaptors act in a non-redundant manner. In cellular immunostaining experiments, GRASP55 localized to perinuclear Golgi regions. Notably, upon UPS activation by ARF1-Q71L, GRASP55 redistributed toward peripheral structures, likely tubular ER regions, leading to a marked increase in its co-localization with ΔF508-CFTR (from 22% to 68%, Supplementary Fig. 4), consistent with previous findings[12,36]. Interestingly, activation of the UPS by ARF1-Q71L did not significantly increase its co-localization with SNX27, despite the peripheral redistribution of GRASP55 (Fig. 5e, f). Taken together, these findings imply that GRASP55 and SNX27 contribute to the UPS pathway in distinct yet complementary manners, functioning at different stages of the trafficking process.

In addition to SNX27, we examined the potential involvement of SNX2 and SNX17 in the UPS of ΔF508-CFTR, given that these have previously been shown to be involved in the endosomal transport of transmembrane protein cargos[37,38]. SNX2 is a member of SNX-BAR (Bin/Amphiphysin/Rvs) proteins, which are responsible for tubular-based endosomal sorting, and it has been shown to interact with SNX27[37]. Furthermore, SNX2 has been implicated in ER-endosome contact regulation, which may be relevant for promoting Golgi-bypass trafficking[39]. Similarly to SNX27, SNX17 possesses PX and FERM domains; however, it lacks the PDZ and is known as an adaptor for PDZ-independent endosomal recycling pathways[38,40]. While SNX2 gene knockdown resulted in reduced ΔF508-CFTR surface expression via UPS, SNX17 knockdown did not (Supplementary Fig. 5). These findings suggest that SNX-BAR-related mechanisms may also be involved in this process (see "Discussion") and that the PDZ domain of SNX27 may play a role in CFTR cargo recognition.

Arginine 68 of SNX27 PDZ is a key residue in the VPS26A-SNX27-CFTR assembly

Next, we conducted structural analyses of the interactions involving VPS26A, the SNX27 PDZ domain, and CFTR using the AlphaFold system, along with co-IP and site-directed mutagenesis. We generated VPS26A/SNX27-PDZ models using both AlphaFold2[41] and AlphaFold3[42]. Although the two models were broadly similar, the AlphaFold2-V2 predictions exhibited more favorable confidence metrics, including higher pLDDT scores and lower predicted aligned error values (Supplementary Fig. 6a–d). Ramachandran plot analysis comparing the models with the experimentally determined crystal structure further indicated that the AlphaFold2 model more closely resembled the known structure (Supplementary Fig. 6e–g). Consistent with this, the AlphaFold2-predicted structure of human VPS26A and the SNX27 PDZ domain was nearly identical to the previously reported crystal structure of mouse VPS26A and rat SNX27 PDZ[32], with a root mean square deviation (RMSD) of less than 1 Å (Supplementary Fig. 6h). Based on

https://doi.org/10.1038/s41467-026-71409-9

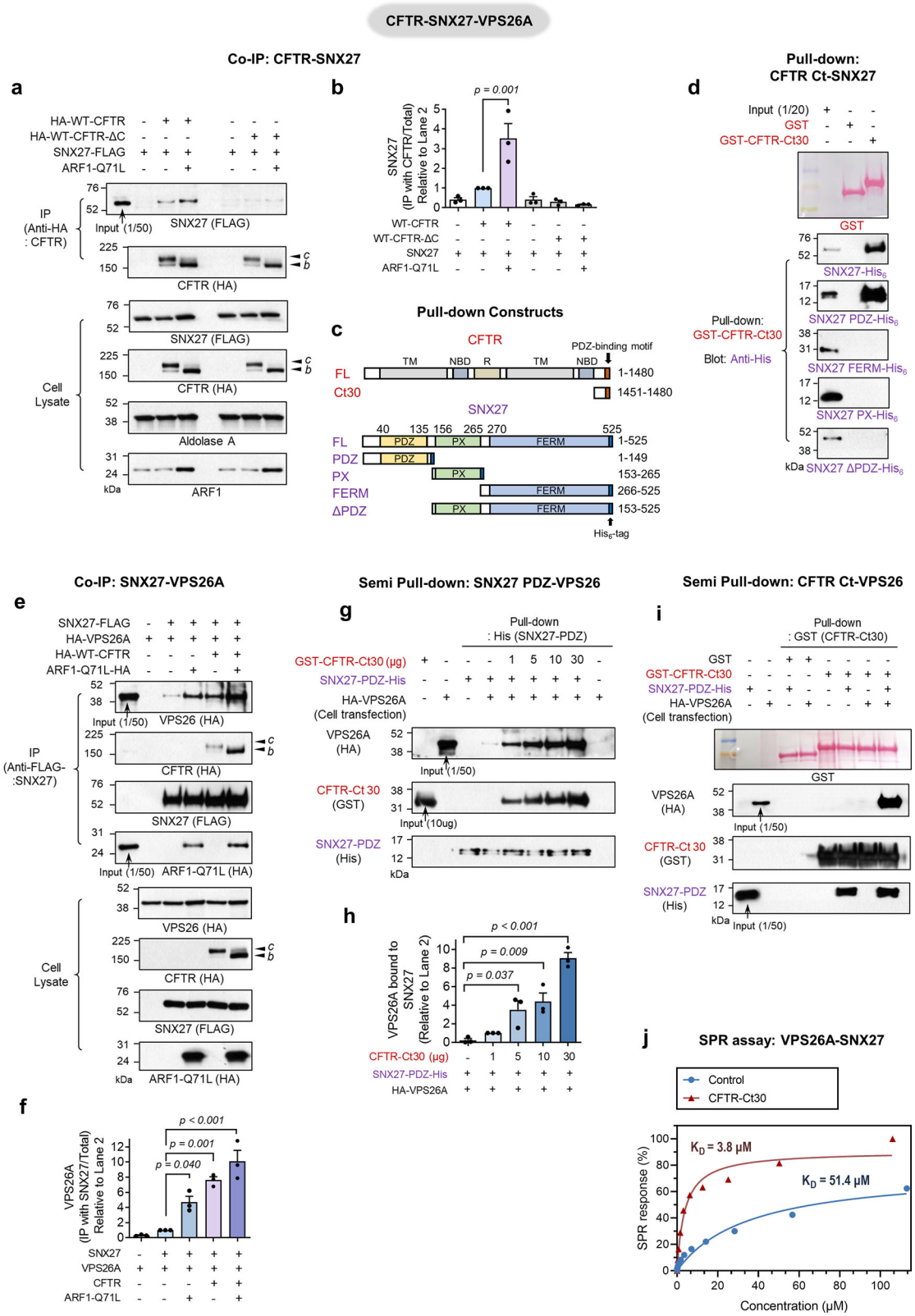

these results, we selected the AlphaFold2-V2 model for all subsequent analyses. We then incorporated CFTR PDZ-binding motif into the structure, and the predicted model showed that the last four residues CFTR "DTRL", known as key residues of the PDZ-binding motif, fit into the binding pocket of the SNX27 PDZ domain (Fig. 6a and Supplementary Data 4 and 5).

After successful construction of the VPS26A/SNX27 PDZ/CFTR PDZ-binding motif assembly, we performed molecular dynamics (MD) simulations to determine whether the binding of CFTR PDZ-binding motif to the SNX27 PDZ domain affected the interaction between VPS26A and SNX27 PDZ. Due to the high intrinsic flexibility of the CFTR C terminus, 6 residues that were stably bound to the SNX27 PDZ

https://doi.org/10.1038/s41467-026-71409-9

Fig. 4 | SNX27 recruits CFTR to the retromer complex through PDZ-based interaction. a, **b** Immunoprecipitation analysis of CFTR and SNX27 interaction. HEK293 cells were transfected with DYK-tagged SNX27 and either HA-tagged WT-CFTR or HA-tagged ΔC-WT-CFTR. In some conditions, ARF1-Q71L was co-expressed to induce UPS (24 h). Immunoprecipitation was performed using anti-HA antibody-conjugated beads, and protein samples were analyzed using immunoblotting. Representative blots and quantification from three independent experiments are shown ($n = 3$). **c** Schematic diagram of CFTR and SNX27 constructs used in pull-down assays. FL full-length, TM transmembrane domain, NBD nucleotide-binding domain, R regulatory domain, PDZ PSD-95/discs large/ZO-1, PX Phox homology, FERM Four-point-one, ezrin, radixin, moesin. **d** Pull-down assay showing the interaction between the His6-tagged SNX27 domains and GST-fused CFTR C-terminal 30 amino acids. Input GST-fused proteins were visualized using Ponceau S staining, and SNX27 domains were detected by immunoblotting with anti-His antibodies. Three independent experiments showed similar results. **e**, **f** Immunoprecipitation analysis of SNX27 and VPS26A interaction. HEK293 cells were transfected with HA-tagged VPS26 or DYK-tagged SNX27, with or without HA-tagged CFTR and ARF1-Q71L co-expression (24 h). Immunoprecipitation was performed using anti-DYK (FLAG) antibody-conjugated beads, followed by immunoblotting. Representative blots are shown in (**e**), with quantification from multiple experiments summarized in (**f**) ($n = 3$). **g**–**i** Semi pull-down assay evaluating the interaction among the C-terminal 30 amino acids of CFTR, the 6 × His-tagged PDZ domain of SNX27, and lysates from HEK293 cells overexpressing HA-tagged VPS26 (24 h). Representative immunoblots are shown in (**g**) (pull-down with SNX27-PDZ) and (**i**) (pull-down with CFTR-C terminus), with quantification from three independent experiments for (**g**) shown in (**h**) ($n = 3$). Three independent experiments of (**i**) showed similar results. **j** Normalized steady-state SPR binding curves showing the interaction of SNX27-PDZ (blue) or SNX27-PDZ pre-incubated with CFTR-Ct30 at a 1:6 molar ratio (red) with immobilized VPS26A on a CM5 sensor chip. The SNX27-PDZ + CFTR-Ct30 complex exhibited higher affinity for VPS26A ($K_D = 3.8$ μM) compared with SNX27-PDZ alone ($_{KD} = 51.4$ μM). Corresponding SPR sensorgrams are shown in Supplementary Fig. 3. Bar graphs show mean ± SEM. All statistical analyses shown in this figure were performed using one-way ANOVA followed by Tukey's multiple comparison test. *b*, core-glycosylated CFTR; *c*, complex-glycosylated CFTR.

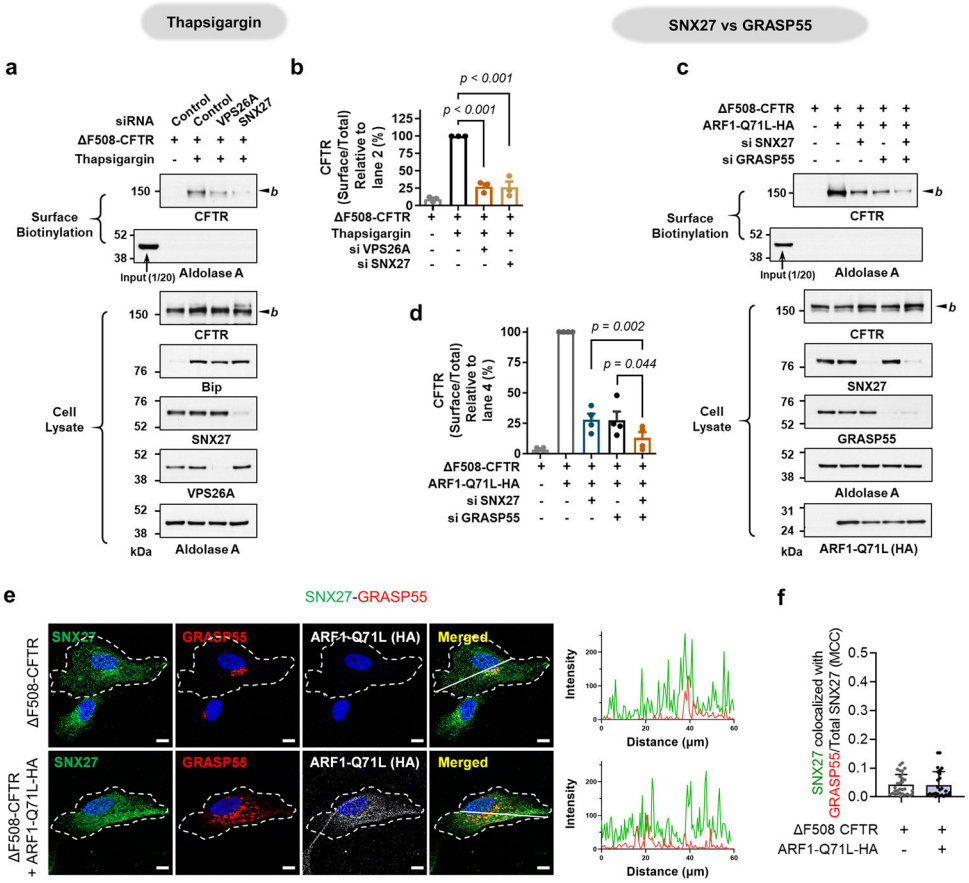

Fig. 5 | SNX27 and GRASP55 contribute to ΔF508-CFTR UPS in a non-redundant manner. a, **b** Cell surface biotinylation assay was performed using HEK293 cells co-transfected with ΔF508-CFTR (40 h) and either control siRNA, VPS26A siRNA, or SNX27 siRNA (100 nM, 60 h), followed by treatment with thapsigargin (5 μM, 6 h) to induce ER stress and activate the unconventional protein secretion (UPS) pathway. Representative immunoblots are shown in (**a**), and quantification of surface-biotinylated CFTR relative to total lysate levels is shown in (**b**) ($n = 3$). Statistical analysis for (**b**) was performed using one-way ANOVA followed by Tukey's multiple comparison test. **c**, **d** Cell surface biotinylation assays were performed using HEK293 cells transfected with control siRNA or siRNAs targeting SNX27 and/or GRASP55 (50 nM, 72 h), followed by ARF1-Q71L expression to induce UPS (48 h). Representative immunoblots are shown in (**c**) (*b*, core-glycosylated CFTR), and quantification from three independent experiments is shown in (**d**) ($n = 4$). Statistical analysis for (**d**) was performed by a two-tailed Student's *t*-test. **e**, **f** HeLa cells expressing ΔF508-CFTR with or without ARF1-Q71L were stained for SNX27 and GRASP55. Representative images (**e**) and Manders' colocalization coefficients (**f**) are shown ($n = 31$ cells for ΔF508-CFTR and $n = 27$ cells for ΔF508-CFTR + ARF1-Q71L, from 3 independent experiments). The white dotted line indicates the regions selected for quantification, and the white straight line in the merged images marks the line used for line-scan analysis with the corresponding intensity profiles shown on the right. Additional representative images are available in Supplementary Fig. 11. Scale bars: 10 μm. Data are mean ± SEM. Statistical significance was assessed by a two-tailed Student's *t*-test.

https://doi.org/10.1038/s41467-026-71409-9

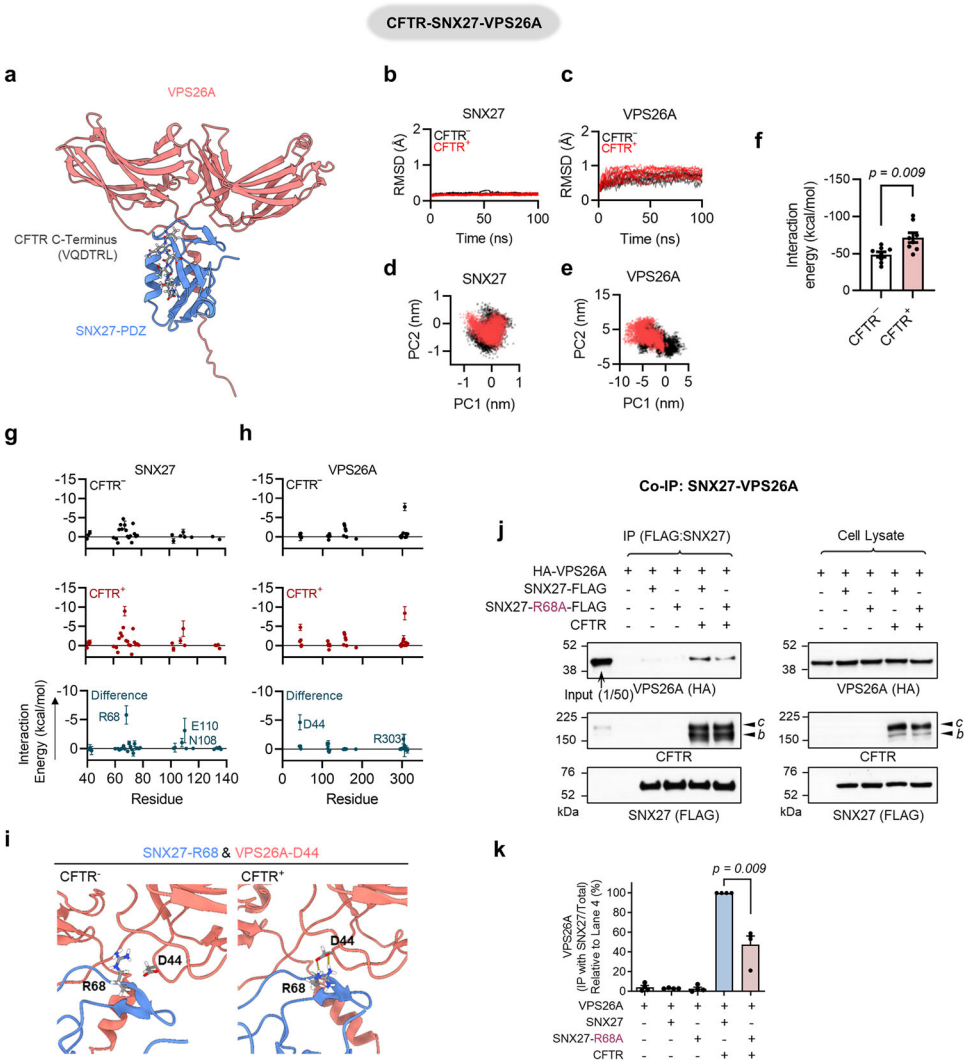

Fig. 6 | Presence of CFTR C-terminus stabilizes the VPS26A-SNX27-CFTR assembly. a Structural model of SNX27 PDZ domain (blue), VPS26A (red), and CFTR C-terminus residues, VQDTRL, predicted by AlphaFold2. **b**–**e** MD simulation analysis (**b**) Root mean square deviation (RMSD) of SNX27 over 100 ns. **c** RMSD of VPS26A over 100 ns. **d** Principal component analysis (PCA) of SNX27 over the last 50 ns. **e** PCA of VPS26A over the last 50 ns. In (**b**–**e**), black lines and dots represent CFTR-absent simulations, while red lines and dots indicate CFTR-present simulations. Eight independent simulations were conducted for each condition. **f** Binding energy analysis. Molecular mechanics with generalized Born and surface area solvation (MM/GBSA) calculations for SNX27-VPS26A binding in the presence and absence of CFTR C-terminus. Statistical significance was determined using a two-tailed Student's *t*-test ($n = 8$). **g**, **h** Residue decomposition analysis (**g**) SNX27 residues contributing to VPS26A interaction. R68, N108, and E110 were identified based on an energy difference cutoff of −0.0 kcal/mol ($n = 8$). **h** VPS26A residues contributing to SNX27 interaction. D44 and R303 were identified using the same cutoff. **i** Molecular representation of SNX27-R68 and VPS26A-D44 interactions in the presence and absence of CFTR. Interactions within 2.5 Å are shown as yellow dotted lines. **j**, **k** Experimental validation of SNX27-VPS26A interaction. Immunoprecipitation was performed using anti-DYK (FLAG) antibody-conjugated beads in HEK293 cells expressing HA-tagged VPS26 and either WT-SNX27 or SNX27-R68A. Representative blots are shown in (**j**), with quantification from four independent experiments in (**k**) ($n = 4$). Bar graphs represent mean ± SEM. Statistical analysis was performed using a two-tailed Student's *t*-test. *b*, core-glycosylated CFTR; *c*, complex-glycosylated CFTR.

domain (VQDTRL) were included for the simulation. Eight independent 100 ns-long MD simulations were conducted with and without CFTR PDZ-binding motif. The RMSD of SNX27 PDZ and VPS26A stabilized after 20 ns of simulation, indicating that the overall protein complex had reached an equilibrated state (Fig. 6b, c). Next, we performed principal component analysis (PCA) separately on SNX27 PDZ and VPS26A during the last 50 ns of the simulation. While the structural distribution of SNX27 PDZ remained largely unchanged with or without CFTR PDZ-binding motif, VPS26A exhibited structural differences in the presence of CFTR PDZ-binding motif (Fig. 6d, e). To further investigate the interaction between VPS26A and SNX27 PDZ, we calculated their interaction energies using the molecular mechanics with generalized Born and surface area solvation (MM/GBSA) method[43]. Notably, in the presence of CFTR PDZ-binding motif, the interaction energy between VPS26A and SNX27 PDZ increased significantly (Fig. 6f), which was consistent with the co-IP and pull-down experiments showing that CFTR PDZ-binding motif enhanced VPS26A-SNX27 interaction (Fig. 4e–i).

To identify key residues responsible for the increased interaction, we performed residue decomposition analysis based on the MM/GBSA results. By comparing the interaction energy differences in the absence and presence of CFTR PDZ-binding motif (Fig. 6g, h), we identified R68, N108, and E110 in SNX27 PDZ as residues that interacted more strongly with VPS26A when CFTR PDZ-binding motif was present. Similarly, in VPS26A, D44 and R303 were identified as residues responsive to the CFTR PDZ-binding motif. As illustrated in Fig. 6i, R68 from SNX27 and D44 from VPS26A were positioned closely, forming a salt bridge that stabilizes the interaction interface. To assess the

functional relevance of these predicted interactions, we experimentally validated the VPS26A-SNX27-CFTR interaction using the SNX27-R68A mutant (Fig. 6j, k), as R68 exhibited the greatest difference in interaction energy in the presence and absence of the CFTR PDZ-binding motif (Fig. 6g, h). Co-IP experiments in HEK293 cells expressing whole proteins of VPS26A, SNX27, and CFTR revealed that the SNX27-R68A substitution significantly reduced the interaction between VPS26A and SNX27 in the presence of CFTR (Fig. 6j, k), consistent with the MD simulation results.

VPS26A, SNX27, and RAB11A contribute to anterograde CFTR trafficking via the UPS

The steady-state cell-surface abundance of CFTR proteins observed in surface biotinylation experiments reflects a dynamic equilibrium among: (1) newly synthesized proteins arriving at the plasma membrane via anterograde transport, (2) retrograde removal through endocytosis, and (3) recycling of endocytosed proteins back to the cell surface. In contrast to wild-type CFTR, for which approximately 40% of endocytosed proteins are recycled in 10 min, recycling of cell-surface rescued ΔF508-CFTR is markedly reduced (~5% in 10 min) due to peripheral protein quality control-mediated ubiquitination and subsequent lysosomal targeting[44]. Therefore, inhibition of endocytic removal largely reflects de novo anterograde transport in the case of ΔF508-CFTR. Accordingly, to minimize the contribution of endocytic retrieval to cell-surface abundance and to more accurately interpret CFTR surface delivery under UPS-inducing conditions, we inhibited endocytic removal using dynasore, a dynamin GTPase inhibitor that blocks clathrin- and dynamin-dependent endocytosis[45], and assessed the effects of retromer and SNX27 silencing. Treatment with dynasore increased the cell-surface expression of ΔF508-CFTR induced by ARF1-Q71L (Fig. 7a, b), which correlates with the previous report that endocytic removal of cell-surface ΔF508-CFTR is augmented due to the peripheral quality control systems[44]. Importantly, knockdown of VPS26A or other retromer complex components still significantly reduced surface levels of ΔF508-CFTR even under dynasore treatment (Fig. 7a, b), indicating that the VPS26A-SNX27 complex contributes to an anterograde route to promote Golgi-bypass delivery of CFTR to the plasma membrane. Unlike the UPS of ΔF508-CFTR, the conventional Golgi-mediated trafficking of wild-type CFTR was not significantly affected by silencing of retromer complex components (Fig. 7c, d), highlighting the specificity of the complex in the UPS pathway.

To better understand the directionality and vesicular route of this anterograde trafficking, we examined whether the CFTR UPS involves recycling endosomes. Specifically, we investigated the role of Rab11A, a well-characterized regulator of canonical recycling endosomes[46]. As shown in Supplementary Fig. 7, RAB11A knockdown significantly reduced ARF1-Q71L-induced UPS of both WT- and ΔF508-CFTR (band B), while leaving conventional WT-CFTR trafficking (band C) largely unaffected. Notably, the effect of RAB11A silencing persisted under dynasore-treated conditions, providing further evidence for the involvement of Rab11A-mediated transport in ΔF508-CFTR UPS (Fig. 7e, f).

UPS activation by ARF1-Q71L increased the spatial overlap between ΔF508-CFTR and Rab11A (Fig. 7g, h), and similar trends were observed under additional UPS-inducing conditions, including STX5 or SAR1-T39N overexpression and thapsigargin treatment (Fig. 7h and Supplementary Fig. 8). Likewise, UPS induction also increased overlap between SNX27 and Rab11A (Fig. 7i, j and Supplementary Fig. 9). Collectively, these results suggest increased engagement of Rab11A-positive recycling compartments during stress-induced Golgi-bypass of ΔF508-CFTR.

VPS26A and SNX27 participate in the UPS of SARS-CoV-2 spike protein

We next examined the roles of VPS26A and SNX27 in the intracellular trafficking of the viral envelope protein SARS-CoV-2 spike, which plays a critical role in host cell entry[16]. The spike protein can be cleaved into S1 and S2 fragments by furin, a cellular protease predominantly present in the Golgi apparatus[47]. Thus, the presence of cleaved spike at the plasma membrane or the viral envelope is consistent with Golgi-mediated transport, whereas the presence of uncleaved spike is compatible with Golgi-independent trafficking. Notably, it has been reported that authentic SARS-CoV-2 particles contain substantial amounts of uncleaved spike protein, and that the spike protein can be transported via a Golgi-bypass pathway[15,19,48]

When the spike protein is exogenously expressed in HEK293 cells using plasmid vectors under non-stress inducing conditions, the majority of cell surface-expressed spike proteins are cleaved, indicating that they have been transported via a Golgi-mediated route (Fig. 8a). Silencing VPS26A or SNX27 had no effect on the Golgi-dependent surface trafficking of these cleaved spike proteins (Fig. 8a, b), suggesting that VPS26A and SNX27 are dispensable for this conventional Golgi-dependent route. We then examined whether VPS26A and SNX27 are required when UPS is activated by blockade of ER-to-Golgi trafficking. Blocking ER-to-Golgi trafficking with ARF1-Q71L induced Golgi-independent cell surface expression of uncleaved spike protein (Fig. 8c). Notably, knockdown of VPS26A or SNX27 significantly reduced the surface delivery of uncleaved spike (Fig. 8c, d), indicating that VPS26A and SNX27 are required for Golgi-bypass trafficking of the spike protein. The effects of VPS26A and SNX27 silencing remained unchanged following dynasore treatment, similar to that observed for ΔF508-CFTR UPS.

We next assessed the physiological relevance of these findings using authentic SARS-CoV-2 infection in HeLa-ACE2 cells. Authentic SARS-CoV-2 viral particles harvested from the supernatant of HeLa-ACE2 cells infected with SARS-CoV-2 contain a substantial proportion of uncleaved spike proteins. Notably, the silencing of VPS26A or SNX27 resulted in a significant reduction in uncleaved spike proteins in viral particles (Fig. 8e, f). To determine the pathophysiological impact of reducing spike protein content in viral particles, a virus plaque assay was performed. Inhibition of either VPS26A or SNX27, or their combined inhibition, resulted in decreased levels of active virus secretion (Fig. 8g). Additionally, analysis of secreted viral mRNA levels showed results consistent with those of the plaque assay (Fig. 8h). A recent report suggests that SNX27 affects SARS-CoV-2 infection by inhibiting cell surface expression of the viral receptor protein ACE2[49]. However, in our system, VPS26A or SNX27 knockdown did not alter ACE2 surface expression (Supplementary Fig. 10). Taken together, these findings indicate that VPS26A- and SNX27-mediated UPS of the spike protein contributes to maintaining proper viral infectivity and replication of SARS-CoV-2.

Discussion

The retromer complex, composed of VPS26, VPS29, and VPS35, functions as a key element of protein sorting and endosomal trafficking. It interacts with a diverse array of SNXs, and its role in intracellular pathways depends on the specific SNXs involved[22]. Initially identified as a mediator of retrograde transport for transmembrane cargo proteins from endosomes to the trans-Golgi network, the retromer has since been found to participate in other intracellular trafficking processes, including the recycling of cargo proteins in conjunction with specific SNXs, such as SNX27[24].

The present study reveals an unidentified role for retromer and SNX27 in the unconventional trafficking of transmembrane proteins such as CFTR and the spike protein of SARS-CoV-2 (Fig. 9). As a cargo adaptor, SNX27 binds to CFTR via PDZ-based interaction, facilitating the association between the VPS26A retromer complex and CFTR. Notably, the binding affinity between SNX27 and VPS26A increases in the presence of CFTR (Fig. 4). In silico predictions and molecular confirmation via site-directed mutagenesis provide an explanation for this result, demonstrating that the interaction

https://doi.org/10.1038/s41467-026-71409-9

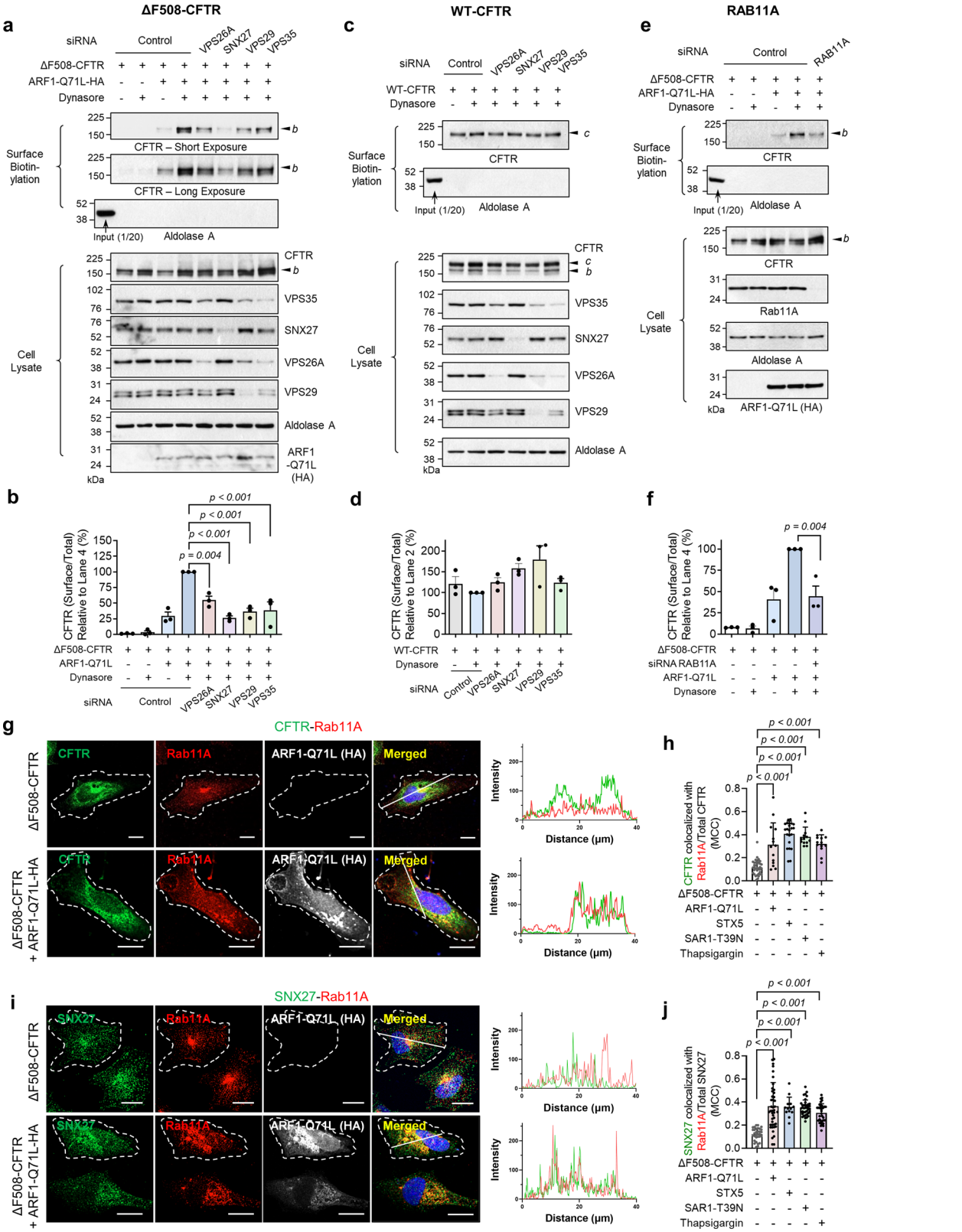

energy between VPS26A and the PDZ domain of SNX27 increases when the C-terminus of CFTR binds to the SNX27 PDZ pocket (Fig. 6). These findings suggest that cargo proteins can stabilize the interaction between SNXs and the retromer, thereby contributing to membrane coat formation. Interestingly, silencing the SNX-BAR protein SNX2 also reduces ΔF508-CFTR UPS (Supplementary Fig. 5). SNX2 contains a BAR domain, which can sense membrane curvature and induce membrane tubulation, and is a component of the endosomal SNX-BAR sorting complex for promoting exit 1 (ESCPE-1) transport carriers[50]. It has been proposed that the SNX27 FERM domain directly binds to SNX2, and that this interaction is required to transfer the cargo proteins to the ESCPE-1 transport carrier to facilitate endosome-to-plasma membrane recycling[37]. Further investigation into the roles of membrane tubulation and ESCPE-1

https://doi.org/10.1038/s41467-026-71409-9

Fig. 7 | Retromer, SNX27, and RAB11A contribute to anterograde CFTR trafficking via the UPS. a–f Cell surface biotinylation assay. HEK293 cells were transfected with control siRNA or specific siRNAs (50 nM, 48 h) along with ΔF508-CFTR plasmids (24 h). In some conditions, ARF1-Q71L was co-expressed to induce ER stress, and dynasore (80 μM, 2 h) was used to inhibit endocytosis. Representative immunoblots are shown in (**a**, **c**, **e**), with quantification from three independent experiments in (**b**, **d**, **f**) ($n = 3$), respectively. *b*, core-glycosylated CFTR; *c*, complex-glycosylated CFTR. **g–j** Immunofluorescence analysis of SNX27, Rab11A, and ΔF508-CFTR. HeLa cells were transfected with ΔF508-CFTR, with or without ARF1-Q71L-HA, STX5-HA, SAR1-T39N-MYC, or treated with thapsigargin (3 μM, 4 h), and stained with anti-CFTR, anti-Rab11A, anti-SNX27, and anti-HA antibodies. Representative confocal images of ΔF508-CFTR and Rab11A (**g**) and SNX27 and Rab11A (**i**) in cells expressing ARF1-Q71L are shown. The white dotted line indicates the regions selected for quantification, and the white straight line in the merged images marks the line used for line-scan analysis with the corresponding intensity profiles shown on the right. Additional representative images are available in Supplementary Fig. 11. Images under additional UPS-inducing conditions (STX5, SAR1-T39N, and thapsigargin) are presented in Supplementary Figs. 8 and 9. Nuclei were stained with DAPI. Manders' co-localization coefficients (MCC) for ΔF508-CFTR with Rab11A (**h**; $n = 36$ cells for ΔF508-CFTR, $n = 14$ cells for ΔF508-CFTR + ARF1-Q71L, $n = 22$ cells for ΔF508-CFTR + STX5, $n = 13$ cells for ΔF508-CFTR + SAR1-T39N, and $n = 13$ cells for ΔF508-CFTR + Thapsigargin; from 3 independent experiments) and SNX27 with Rab11A (**j**; $n = 32$ cells for ΔF508-CFTR, $n = 44$ cells for ΔF508-CFTR + ARF1-Q71L, $n = 13$ cells for ΔF508-CFTR + STX5, $n = 39$ cells for ΔF508-CFTR + SAR1-T39N, and $n = 34$ cells for ΔF508-CFTR + Thapsigargin; from 3 independent experiments) are quantified. Scale bar: 20 μm. Bar graphs represent mean ± SEM. All statistical analyses shown in this figure were performed using one-way ANOVA followed by Tukey's multiple comparison test.

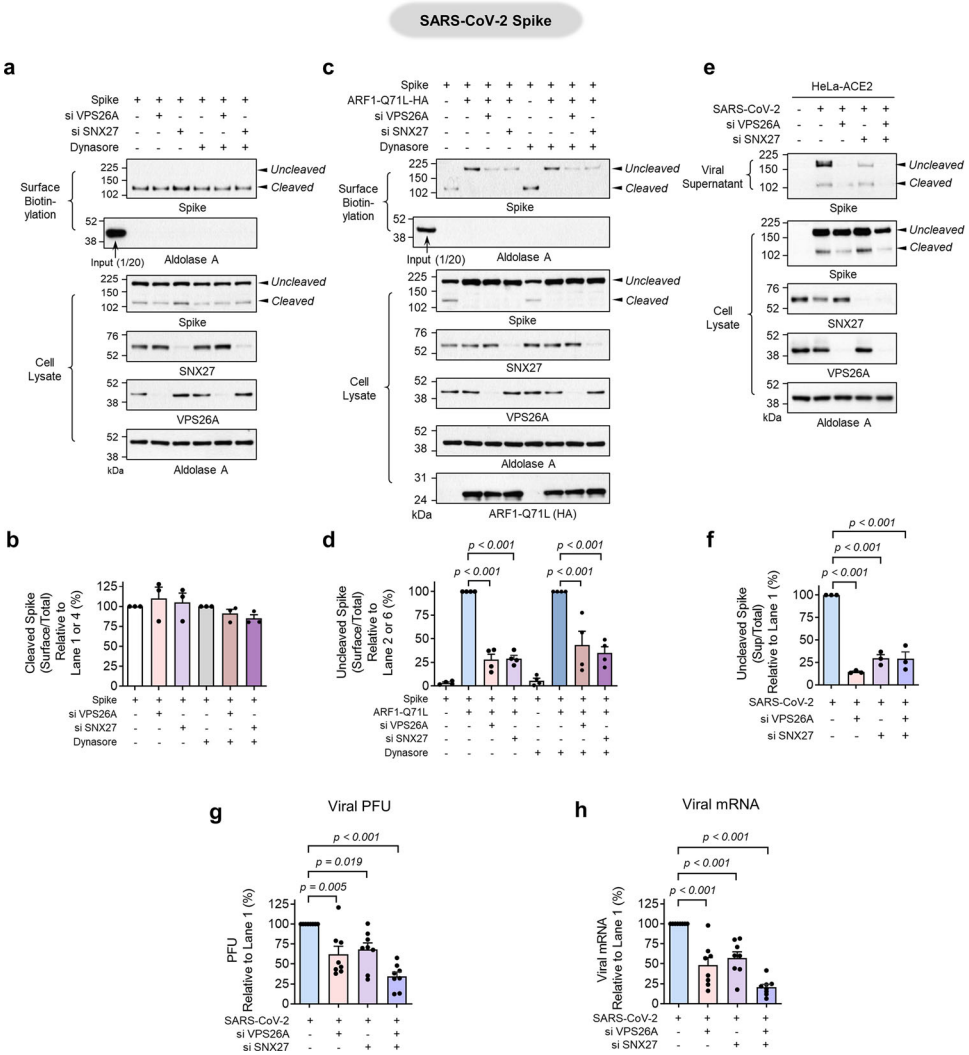

Fig. 8 | VPS26A and SNX27 participate in the Golgi-independent trafficking of SARS-CoV-2 spike protein. a–d Effects of VPS26A and SNX27 silencing on SARS-CoV-2 spike protein trafficking in mammalian cells. HEK293 cells were transfected with control siRNAs, or VPS26A and SNX27 siRNAs (50 nM each, 48 h), along with SARS-CoV-2 spike-expressing plasmids (24 h). In certain conditions, ARF1-Q71L was co-transfected to block ER-to-Golgi trafficking, and dynasore (80 μM, 2 h) was applied to inhibit endocytosis. Cells were then surface biotinylated and analyzed using immunoblotting. Representative blots are shown in (**a**, **c**), with quantifications from multiple experiments summarized in (**b**) ($n = 3$) and (**d**) ($n = 4$), respectively. **e**, **f** Effects of VPS26A and SNX27 silencing on SARS-CoV-2 spike protein levels in viral particles. ACE2-overexpressing HeLa cells were transfected with control siRNAs, or VPS26A and SNX27 siRNAs (50 nM each, 72 h), with SARS-CoV-2 infection following (10 MOI, 24 h). Supernatants and cell lysates were collected for immunoblotting in (**e**), with quantification in (**f**) ($n = 3$). **g**, **h** Viral replication was assessed by measuring viral RNA (vRNA) levels and the infectivity of secreted virus in the culture medium using plaque assays and quantitative PCR. Plaque assay results are shown in (**g**) ($n = 8$), and qPCR data are in (**h**) ($n = 8$). Bar graphs show mean ± SEM. All statistical analyses shown in this figure were performed by one-way ANOVA followed by Tukey's multiple comparison test.

https://doi.org/10.1038/s41467-026-71409-9

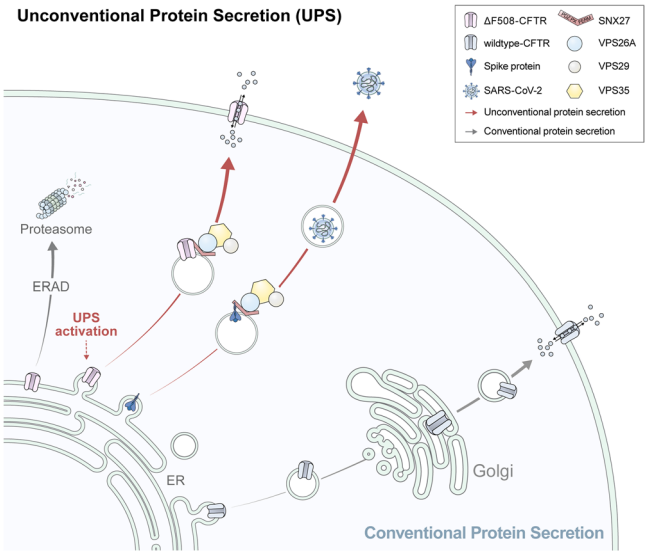

Fig. 9 | Schematic representation of the unconventional protein secretion (UPS) of CFTR and SARS-CoV-2 spike protein mediated by the retromer complex and SNX27. Wild-type (WT) CFTR follows the conventional ER-to-Golgi trafficking pathway to reach the plasma membrane (gray arrow on the right). In contrast, ΔF508-CFTR, which has folding defects, is typically degraded via the ER-associated degradation (ERAD) pathway and fails to reach the membrane (short gray arrow on the left). However, under conditions that activate UPS, both ΔF508-CFTR and WT-CFTR can bypass the Golgi and are transported directly to the plasma membrane (red arrows). This study demonstrates that the retromer complex and SNX27 are key regulators of the UPS pathway for membrane proteins. SNX27 interacts with CFTR via its PDZ domain and associates with VPS26, thereby facilitating the plasma membrane localization of ΔF508-CFTR. Similarly, the retromer complex and SNX27 mediate the Golgi-bypass trafficking of the SARS-CoV-2 spike protein, contributing to viral secretion (red arrows).

would help elucidate the precise mechanistic details of stress-induced UPS of membrane proteins.

Although SNX27 can bind to the C-terminal PDZ-binding motif of wild-type CFTR, knockdowns of SNX27 and VPS26A did not affect its conventional Golgi-mediated trafficking (Figs. 2 and 3). This is likely because the functions of the retromer and SNX27 are not predominant in conventional Golgi-mediated trafficking. Notably, under UPS-inducing conditions, co-localization between SNX27 and ΔF508-CFTR increased (Fig. 3g, h). This finding suggests that cell signals triggered by ARF1-Q71L, such as ER stress-associated IRE1 kinase activation[13], may recruit the cargo adaptor SNX27 to sites where CFTR is clustered, thereby facilitating retromer-mediated trafficking of the cargo protein to the plasma membrane.

The inhibition of endocytosis via dynasore treatment increased the amount of unconventionally cell surface-expressed ΔF508-CFTR (Fig. 7a, b), indicating that a substantial proportion of ΔF508-CFTR undergoes endocytic removal. Silencing VPS26A, VPS29, VPS35, or SNX27 significantly reduced ΔF508-CFTR UPS even under dynasore-treated conditions, further suggesting that these proteins primarily function in anterograde trafficking to the plasma membrane. The involvement of Rab11A also implies the participation of recycling endosomes in UPS. Silencing Rab11A, which is involved in endosomal recycling[46], led to a reduction in CFTR UPS (Fig. 7e, f). In morphological analyses, Rab11A-positive compartments appear to contribute to CFTR surface delivery; however, our imaging data do not necessarily support an obligate functional relationship between SNX27 and Rab11A. Interestingly, SNX27 has been reported to localize to Rab11-marked recycling endosomes and to exhibit coordinated dynamics with Rab11 in neurons[31], whereas other studies have observed limited SNX27-Rab11 overlap in different cellular contexts[51]. These findings suggest that the degree of association between SNX27 and Rab11A may vary depending on cargo and cell type, and that further studies will be required to precisely define their respective contributions to UPS.

Recently, several studies have explored the role of SNX27 in SARS-CoV-2 infection and spike protein trafficking[49,52,53]. These studies primarily focus on the involvement of SNX27 in Golgi-mediated trafficking of the cleaved SARS-CoV-2 spike protein in mammalian cells. However, their findings have been inconclusive and sometimes conflicting. While Zhao et al. have reported that SNX27 participates in the cell surface trafficking of the spike protein[53], Cattin-Ortolá et al. suggest that it does not play a role in the cell surface delivery of the spike protein[52]. In the present study, we show that retromer and SNX27 contribute to the Golgi-independent trafficking of the spike protein, which occurs during authentic virus infection. Gene knockdowns of VPS26A and SNX27 in HeLa-ACE2 cells led to a significant reduction in the levels of uncleaved spike protein in secreted viral particles in infected cells (Fig. 8e, f). This reduction was accompanied by decreases in viral infectivity and replication (Fig. 8g, h). Interestingly, several reports have suggested that Rab11-positive endosomal recycling compartments play a role in the replication of positive-strand RNA viruses, including SARS-CoV-2[54–57], which aligns closely with the findings of this study. Taken together, these results indicate that SARS-CoV-2 hijacks the endosomal recycling machinery of host cells, which is essential for the viral life cycle and replication of SARS-CoV-2, with retromer and SNX27 playing a central role.

A remaining question to be addressed is at which stage of the UPS pathway the retromer and SNX27 act. Based on the finding that the UPS of CFTR proceeds from the ER core-glycosylated form (Fig. 1), it appears that the UPS process begins with vesicle budding from the ER. Recently, an ER-derived tubulovesicular structure termed the ER tubular body, which is enriched in GRASP55, has been shown to play a critical role in vesicle generation during UPS activation[48]. The results of the present study indicate that GRASP55 and SNX27 contribute to the UPS at different stages of the trafficking process (Fig. 5). Therefore, it is conceivable that GRASP55 facilitates the ER exit of ΔF508-CFTR upon UPS activation, particularly at ER tubular bodies, whereas SNX27 participates in the cell-surface trafficking of ΔF508-CFTR from recycling endosomes once the ER-derived vesicles reach the endosomal system. However, since retromer and SNX proteins have the capability to induce membrane tubulation[22], it will be of interest to determine whether the VPS26A retromer complex and SNX27 are also involved in the formation of tubular structures and vesicles within the ER tubular body.

Additionally, it will also be an interesting endeavor to investigate whether the retromer and SNX proteins provide a major common route for stress-induced UPS, including the UPS of cytosolic proteins, which is associated with the pathogenesis of many human diseases under cellular stress conditions[23]. It is generally accepted that cellular stress conditions, particularly ER stress, activate the UPS[5,13]. However, ER stress itself can be detrimental to the pathogenesis of cystic fibrosis[58]. Therefore, it is highly advisable not to directly induce cellular stress, but rather to rescue cell-surface expression of ΔF508-CFTR through specific activation of the UPS without causing stress, following molecular identification of the UPS machinery. For example, based on the present findings, selective activation of the SNX27-retromer pathway without inducing cellular stress may represent a potential therapeutic approach, particularly when combined with interventions that enhance ER exit of ΔF508-CFTR. Additionally, selective inhibition of this pathway may be beneficial for treating infections caused by viruses that exploit the endosomal recycling machinery for their life cycle, such as SARS-CoV-2. The identification of retromer and SNX27 as UPS factors deepens our understanding of its mechanisms and provides a broader perspective for the investigation of UPS-related diseases, thereby supporting future therapeutic development.

Methods

Cell culture, plasmids, siRNAs, and transfection

HEK293T cells (ATCC, CRL-3216), HEK293 cells (ATCC, CRL-1573) and HeLa cells (ATCC, CCL-2) were obtained from the American Type Culture Collection (ATCC). HeLa, HEK293T and HEK293 cells were cultured in Dulbecco's Modified Eagle's Medium (Gibco, #11995-065, Carlsbad, CA, USA) supplemented with 10% fetal bovine serum (Gibco, #26140-079, Carlsbad, CA, USA) and 1% penicillin/streptomycin (Gibco, #15140-122, Carlsbad, CA, USA). The cells were incubated in a 5% CO_2 environment at 37 °C. ACE2-expressing HeLa cells were generated by lentiviral transduction with hACE2-P2A-BSD followed by blasticidin selection (10 μg/mL), as reported previously[59].

Plasmids encoding human pCMV-ΔF508-CFTR, pCMV-WT-CFTR (pCMVNot6.2), HA- ΔF508-CFTR, HA-WT-CFTR, HA-ΔC-WT-CFTR, pGEX-4T1-CFTR-Ct-30, Myc-SAR1-T39N, HA-Syntaxin5 and mammalian expressible extracellular-tagged full-length HA-ΔF508-CFTR have been described previously[12]. The coding sequence for human ARF1-Q71L was synthesized and incorporated into the pcDNA3.1-HA vector using NEBuilder HiFi DNA Assembly Kit (NEB Biolabs) with a Myc-tag or HA-tag. The commercially obtained vectors pCMV6-VPS26-GFP and pCMV-SNX27-GFP (Origene #NM_004896, #NM_030918, Rockville, MD, USA) contained the coding sequences for VPS26 and SNX27, which were inserted into the pCMV6-Entry-Myc-DYK vector using the BamHI and XhoI restriction enzyme sites. To generate HA-VPS26 construct, the sequence for VPS26 was amplified from pCMV6-VPS26-GFP and the amplicons were cloned into pcDNA3.1-HA vector using the EcoRI and XhoI restriction enzyme sites. To create domain-specific SNX27 constructs with a His6 tag, the PCR fragments (full-length SNX27 [a.a. 1–525], PDZ [a.a. 1–149], PX [a.a. 153–265], FERM [a.a. 266–525], and ΔPDZ [a.a. 153–525]) were inserted into the pET-28a (+) by using the NcoI and XhoI restriction enzyme sites. The SNX27-R68A mutant construct was generated using the Q5® Site-Directed Mutagenesis Kit (New England Biolabs, #E0554S) with the forward primer 5′- CGG GCA ACT GGC GAG CAT CAA CGG GGA G -3′, and reverse primer 5′- CCC TCG CTC ACT TGG CCC CGC ACG TTG AA -3′. The mammalian expressible pcDNA3.1-spike plasmid was generated by inserting a stop codon before the C9 tag of a pcDNA3.1-SARS2-spike plasmid (Addgene #145032). The plasmids were transfected into HeLa and HEK293 cells using either Lipofectamine LTX Reagent (Invitrogen, #15338-100, Carlsbad, CA, USA), TransIT-X2 Dynamic Delivery System (Mirus Bio LLC, #MIR6006, Madison, WI, US), or JetPRIME Reagent (Polyplus, #101000001, Illkirch-Graffenstaden, France), following the manufacturer's protocol. siRNAs (Supplementary Data 8) were transfected into HEK293 cells or ACE2-overexpressing HeLa cells using RNAiMAX transfection reagent (Invitrogen, #13778-150, Carlsbad, CA, USA), following the instructions provided by the manufacturer. All newly generated plasmids are available from the corresponding author upon reasonable request.

High-throughput genetic screening using CRISPR/Cas9 knock-out library

To generate HeLa cell lines expressing Cas9 stably, HEK293T cells were co-transfected with the lentiCas9-Blast plasmid, psPAX2 packaging plasmid, and the pMD2.G envelope plasmid using the TransIT-X2® Dynamic Delivery System (Mirus Bio LLC, #MIR6006) as per the manufacturer's instructions. Subsequently, the HeLa cells were transduced with lentiviral particles obtained from supernatants of HEK293T cells expressing Cas9. After 24 h, the supernatant was replaced with complete medium supplemented with 3 μg/mL blasticidin, and the cells were incubated for an additional 48 h.

For genetic screening, customized sgRNA libraries targeting 1082 genes expected to be involved in UPS were selected and generated. As indicated in Supplementary Fig. 1b, eight sgRNA sequences for each gene were obtained from the Brunello library (https://portals.broadinstitute.org/gppx/crispick/public) as the default option, while the remaining four were designed using an online tool called GUIDES provided by the Sanjana Lab, the Genome-Scale CRISPR Knock-Out (GeCKO) library (https://www.addgene.org/pooled-library/zhang-human-gecko-v2), or CRISPR knockout (CRISPRko) library (https://portals.broadinstitute.org/gpp/public/analysis-tools/sgrna-design). The sgRNA sequences and sources for all genes are provided in Supplementary Data 2.

Lentiviral pooled sgRNA library was prepared, as previously described in detail[60]. To obtain lentiviral particles, libraries were co-transfected with the psPAX2 packaging plasmid and the pMD2.G envelope plasmid into HeLa-Cas9 stable cells. After 24 h, the supernatant was replaced with a complete medium supplemented with 3 μg/mL puromycin for selection. HeLa cells expressing Cas9 were transduced with a lentiviral pooled sgRNA library at a multiplicity of infection (MOI) of approximately 0.3. This process enabled each cell to receive a single sgRNA. Subsequently, the cells were subjected to a six-day puromycin selection process.

After 48 h, stable cells were transfected with CFTR plasmids tagged with the human influenza hemagglutinin (HA) at the extracellular loop region. Unconventional secretion of CFTR protein was induced by co-expression of the ARF1-Q71L, as previously reported[12]. After 24 h, cells were fixed with a 4% paraformaldehyde solution for 10 min, and then washed twice with FACS buffer containing 10% FBS in PBS. The cells were stained with the PE-conjugated anti-HA antibodies (BioLegend, #901517, San Diego, CA, USA) for 1 h at 37 °C, followed by three washes with FACS buffer. Cells expressing CFTR at the cell surface were collected by flow cytometry. Debris and cell clumps were excluded based on forward scatter area (FSC-A) and side scatter area (SSC-A) profiles. Single cells were then identified by gating on forward scatter height (FSC-H) versus forward scatter area (FSC-A). Within the singlet population, the frequencies of HA-positive and HA-negative cells were determined. Data were acquired using a FACS sorter (BD FACS Aria III, Franklin Lakes, New Jersey, USA) and analyzed using FlowJo software (BD Biosciences, Franklin Lakes, New Jersey, USA). Subsequently, genomic DNA was extracted from the obtained cells using the GeneRead DNA FFPE Kit (Qiagen, #180134, Hilden, Germany) following the instructions provided by the manufacturer. The obtained genomic DNA was amplified using polymerase chain reaction with NEB Next® High-Fidelity 2× PCR Master Mix (New England Biolabs, #M0541, MA, USA). Barcoded NGS libraries were generated using a two-step PCR strategy following the protocol described by Joung et al.[60]. The resulting amplicons were purified using the QIAquick Gel Extraction Kit (Qiagen, #28706, Valencia, CA, USA) and sequenced on an Illumina NovaSeq 6000 platform. NGS data were analyzed using MAGeCK (version 0.5.4), and gene enrichment/depletion was assessed with the MAGeCK test based on the robust rank aggregation (RRA) framework. sgRNA-level *p*-values were estimated using a negative binomial model comparing treatment and control read counts. Gene-level *p*-values were then derived by α-RRA ranking of significant sgRNAs followed by permutation testing.

RNA extraction and quantitative polymerase chain reaction (qPCR)

Cellular RNA was extracted using an RNA extraction kit (Bioneer, #K-3140, Daejeon, Korea) following the provided instructions. Subsequently, cDNA synthesis from the isolated RNA was carried out using cDNA EcoDry Premix (Takara, #639549, San Jose, CA, USA) in accordance with the manufacturer's guidelines.

Quantitative PCR (qPCR) was conducted using the Applied Biosystem StepOne System (Applied Biosystems, Forster City, CA, USA). The real-time PCR reactions were quantified by detecting the binding of fluorescent SYBR Green dye to double-stranded DNA. For PCR amplification, the total reaction volume was set to 20 μL with RNase-free water, after combining with 100 ng of cDNA, 2 μL of primer sets, 10 μL of 2× SYBR premix Ex Taq, ROX Plus (Takara, #RR42LR). The amplification protocol included an initial step of incubation at 95 °C for 15 min, followed by 40 cycles at 95 °C for 15 s, and 60 °C for 40 s.

Each cDNA was analyzed in duplicate. Relative mRNA expression levels were normalized to the housekeeping gene GAPDH, and the ΔCt value was determined as follows: ΔCt = Ct (GAPDH) − Ct (target gene). The average ΔCt was subtracted from each experimental condition to obtain the ΔΔCt value. Fold changes in gene expression were calculated as $2^{-\Delta\Delta Ct}$ relative to the control sample, normalized to GAPDH. The primer sequences used in qPCR for each gene are listed in Supplementary Data 5.

Surface biotinylation and immunoblotting

To conduct the biotinylation assay, HEK293 cells cultured in 0.02 mg/mL poly-D-lysine (Sigma Aldrich, #P6407)-coated 6-well plates were incubated for 5 min at 4 °C and washed twice with cold phosphate-buffered saline (PBS). The transmembrane proteins of the cells were biotinylated using Sulfo-NHS-SS-Biotin (Thermo Scientific, #21331, Waltham, MA, USA) in cold PBS (0.3 mg/ml biotin in PBS) on ice for 30 min in darkness. Subsequently, the cells were treated with a quenching buffer consisting of 1% BSA in 0.5× PBS for 10 min on ice in darkness, followed by two washes with cold PBS. The cells were then collected using a lysis buffer containing 150 mM NaCl, 20 mM Tris (pH 7.4), 1 mM EDTA, 1% (v:v) NP40, 0.5% (v:v) sodium deoxycholate, and a protease inhibitor (Roche, #04693159001, Mannheim, Germany). The harvested cells were homogenized using a sonicator for 20 s and centrifuged at 16,000 × *g* for 20 min at 4 °C. The supernatant of the lysate was collected, and 300 μg of the lysate was incubated overnight at 4 °C with 200 μl of 10% streptavidin agarose resin (Thermo Scientific™, #20349, Waltham, MA, USA). The resin bound to the biotinylated proteins was then subjected to centrifugation and washed four times using lysis buffer. The biotinylated proteins were eluted with 2× sodium dodecyl sulfate (SDS) sample buffer containing dithiothreitol (DTT, 0.02 g/ml) at 38 °C for 30 min and subsequently separated through SDS-polyacrylamide gel electrophoresis (PAGE). The separated proteins were transferred to a nitrocellulose membrane (GE Healthcare, Amersham, #10600004, Chicago, IL, USA), and the membrane was blotted using suitable primary antibodies and HRP-conjugated secondary antibodies in 5% skim milk. Protein bands were visualized using enhanced chemiluminescence (GE Healthcare, Amersham #RPN2105), and the density of each protein band was quantified with imaging software (Multi Gauge ver. 3.0; Fujifilm, Tokyo, Japan).

Immunoprecipitation assay

The cells were washed twice with cold phosphate-buffered saline (PBS). Subsequently, the cells were harvested using lysis buffer consisting of 150 mM NaCl, 20 mM Tris (pH 7.4), 1 mM EDTA, 1% (v:v) NP-40, and a protease inhibitor (Roche, #04693159001, Mannheim, Germany). The harvested cells were then homogenized using a sonicator for 20 s and centrifuged at 16,000 × *g* for 20 min at 4 °C. The supernatant of the lysate was collected, and 400 μg of the lysate was incubated for 16 h at 4 °C with 200 μl of lysis buffer containing 5% EZview™ red anti-HA affinity gel (Millipore, #E6779, Billerica, MA, USA). The resin bound to the protein was subjected to centrifugation, washed four times with lysis buffer, and eluted using 2× SDS sample buffer containing dithiothreitol (DTT, 0.02 g/ml) at 38 °C for 30 min. Subsequently, the eluate was separated by SDS-PAGE and subjected to immunoblotting as previously described.

Immunofluorescence assay

HeLa cells were cultured on 18-mm round coverslips. Subsequently, the cells were fixed using a solution of 4% paraformaldehyde for 7 min, and then permeabilized with 0.2% Triton ×-100 in PBS for 5 min. Then, the cells were washed three times with PBS and incubated with a blocking buffer containing 1% BSA and 5% horse serum for 1 h at room temperature. Following the blocking step, the cells were exposed to the appropriate primary antibodies for 1 h at room temperature, and then washed three times with PBS. Subsequently, the cells were stained with fluorescent-dye conjugated secondary antibodies for 30 min at room temperature, and again washed three times with PBS. The following antibodies were used for staining: anti-CFTR ACL006 (Alomone Labs, #ACL006), anti-SNX27 (Abcam, #ab77799), anti-HA (Novus #NB600-362), Alexa Fluor 488-conjugated polyclonal donkey anti-rabbit (Invitrogen, #A21206), Alexa Fluor 568-conjugated polyclonal donkey anti-mouse (Invitrogen, #A10037), and Alexa Fluor 680-conjugated polyclonal donkey anti-goat (Invitrogen, #A21084) antibodies. The sample was mounted onto a slide glass using a mounting medium (Agilent Dako, #S3025, Santa Clara, CA, USA), and the images were captured using a confocal microscope (LSM 980, Carl Zeiss, Berlin, Germany) equipped with a 63×/1.4 numerical aperture oil objective lens.

The degree of colocalization between CFTR, SNX27, and Rab11A was assessed using Manders' colocalization coefficients (MCC), using the colocalization module of the ZEN 2012 software (black edition; Carl Zeiss, Berlin, Germany). For measuring MCC under each condition, pixels with fluorescence intensity above the threshold level of 50 in both channels (red and green) were considered to represent overlapping signals. Subsequently, the mean MCC from the regions of interest was determined. For the two target proteins, referred to as A and B, two distinct MCC values were computed as follows:

$$\text{MCCA colocalized with B/Total A} = \Sigma iAi,\text{colocal}/\Sigma iAi \quad (1)$$

$$\text{MCCB colocalized with A/Total B} = \Sigma iBi,\text{colocal}/\Sigma iBi \quad (2)$$

To visualize spatial colocalization between channels, line-scan intensity profiles were generated using ZEN v3.12 Blue edition (Blue edition; Carl Zeiss, Berlin, Germany). Straight lines were drawn across representative regions containing overlapping fluorescence signals in both channels (red and green) merged images. Fluorescence intensity values (0–255) along the line were extracted for each channel and plotted as a function of distance using GraphPad Prism (GraphPad Software).

Pull-down assay

The Rosetta BL-21(DE3) strain of *Escherichia coli* (Enzynomics, #CP1010, Daejeon, Korea) was used for the production of recombinant proteins. Expression of the recombinant fusion proteins was induced by adding 0.5 mM isopropyl β-D-1-thiogalactopyranoside (IPTG) and followed by incubation at 30 °C for 6 h. The proteins were subsequently purified using either Glutathione Sepharose™ beads (GE Healthcare, #17-0756, Chicago, IL, US) or nickel-nitrilotriacetic acid (Ni-NTA) agarose beads (QIAGEN, #30210, Valencia, CA), according to the manufacturer's instructions. For the pull-down assay, the buffer containing His6-fusion proteins was dialyzed against a buffer composed of 50 mM Tris (pH 7.4), 150 mM NaCl, and 0.05% (v:v) NP40. Subsequently, 10 μg of the eluted His6-fusion proteins were incubated with Glutathione Sepharose™ beads pre-loaded with GST-fusion proteins overnight at 4 °C. The protein-bound beads were washed four times with the dialysis buffer and subsequently eluted in 2× SDS sample buffer. The eluted proteins were subjected to immunoblotting, following the previously described protocol.

Surface plasmon resonance (SPR) analysis

The cDNA fragments encoding the PDZ domain (residues 1–149) of human SNX27 (UniProt: Q96L92) and the full-length human VPS26A (residues 1–327; UniProt: O75436) were cloned into the pET28a vector with an N-terminal 6 × His tag. The construct pET28a-6×His-SNX27-PDZ was transformed into *E. coli* BL21(DE3) cells and cultured in LB medium at 37 °C until the optical density at 600 nm (OD_{600}) reached 0.5–0.6. Protein expression was induced with 0.5 mM IPTG and carried out at 17 °C overnight. Similarly, the pET28a-6×His-VPS26A construct was transformed into *E. coli* C41(DE3) cells, induced at OD_{600} = 0.5–0.6 with

0.3 mM IPTG, and expressed at 17 °C overnight. The cells were harvested by centrifugation at 3000 × *g* for 15 min and stored at −80 °C until use.

For purification, the cell pellets were resuspended in lysis buffer containing 20 mM HEPES (pH 7.5), 150 mM NaCl, and 30 mM imidazole, supplemented with DNase I and a protease inhibitor cocktail (500 µM AEBSF, 1 µM E-64, 1 µM leupeptin, and 150 nM aprotinin). Cells were disrupted by sonication and the lysate was clarified by centrifugation at 35,000 × *g* for 60 min at 4 °C, followed by filtration through a 0.45 µm membrane. The supernatant was incubated with Ni-NTA resin (Thermo Fisher Scientific), washed with the same buffer containing 30 mM imidazole, and eluted with buffer containing 300 mM imidazole. Eluted proteins were concentrated using Amicon® Ultra centrifugal filters (10 kDa or 30 kDa MWCO) and further purified by size-exclusion chromatography on a HiLoad 16/600 Superdex 200 prep-grade column (Cytiva) equilibrated with 20 mM HEPES (pH 7.5) and 150 mM NaCl.

All SPR experiments were performed using a Biacore T200 system (Cytiva) equipped with a Series S CM5 sensor chip. Purified VPS26A protein was covalently immobilized onto the chip surface via standard amine coupling according to the manufacturer's protocol. For pH scouting, 10 mM sodium acetate (pH 5.5) was used, and the immobilization level was adjusted to approximately 3900 RU. A reference flow cell was activated and blocked without ligand for background subtraction. Binding experiments were carried out in HBS-EP$^+$ running buffer (10 mM HEPES pH 7.4, 150 mM NaCl, 3 mM EDTA, and 0.05% [v/v] Surfactant P20) at 25 °C. SNX27-PDZ was injected over the VPS26A-immobilized surface either alone or in complex with the CFTR-Ct30 peptide at a PDZ-to-peptide molar ratio of 1:6, at a flow rate of 30 µL min^{-1}. Association and dissociation phases were recorded, and after each cycle the surface was regenerated with 10 mM glycine-HCl (pH 2.0) for 30 s to remove bound analyte. Sensorgrams were reference-subtracted and analyzed using Biacore T200 Evaluation Software. The equilibrium binding responses were fitted to a 1:1 Langmuir model using steady-state affinity analysis to derive the dissociation constant (K_D).

Protein structure prediction

AlphaFold2 and ColabFold were used to construct VPS26A and SNX27 complex[41,61,62]. We used AlphaFold2-multimer-V2 algorithm without template or minimization and 3 recycle number parameters in ColabFold. AlphaFold3 structure prediction was run directly on the AlphaFold3 server (https://alphafoldserver.com/)[42]. The input sequences were as follows: full sequence of human VPS26A; PDZ domain in human SNX27, corresponding to residues 41 to 136; last 30 residues of human CFTR. The last 30 residues of CFTR, when treated as an independent protein chain, did not form any significant secondary structures, nor did independent ColabFold runs suggest a stably bound conformation. This outcome was anticipated, as although AlphaFold2 excels in de novo protein structure prediction, unstructured N- or C-terminal regions or long loops are likely to exhibit significant flexibility, making them challenging to predict accurately[41]. Therefore, we appended the last 30 residues of CFTR to the C-terminus of the SNX27 PDZ domain, introducing a flexible linker consisting of 30 Gly residues. This Gly-linker approach was widely employed prior to the introduction of AlphaFold2-multimer, as it allows for sufficient structural flexibility without disrupting the overall protein conformation[63]. Incorporating the Gly-rich linker in this manner resulted in consistent binding of the CFTR C terminus to the PDZ domain of SNX27. ChimeraX software was used for the three-dimensional visualization of the proteins and calculation of the Ramachandran plot[64].

Molecular dynamics simulations

The predicted structures of VPS26A-SNX27 and VPS26A-SNX27-CFTR C terminus were used as templates for MD simulations. Since only the last four residues of CFTR were stably bound to the SNX27 PDZ domain, we included only the last six residues (VQDTRL) for the CFTR-bound VPS26A-SNX27 interaction analysis.

The system was initially neutralized and solvated in a 150 mM KCl environment using a CHARMM-GUI web server[65,66]. The final system was contained in an ~120 × 120 × 120 Å^3 box, with ~50,000 water molecules and a total of ~160,000 atoms. All the simulations were performed with the CHARMM36m force field and GROMACS software[67,68].

The particle mesh Ewald algorithm was used to evaluate the long-range electrostatic interactions. The van der Waals interactions for a smoothing function were between 10 and 12 Å. The system was minimized using the steepest descent algorithm for 5000 steps. Then, 125 ps equilibration steps were applied to the protein, with the restraints being gradually reduced to zero. A complete electronic evaluation was performed every 2 fs using the SHAKE algorithm[69]. The pressure and temperature were maintained at 1 atm and 298 K throughout the simulation using the Nosé-Hoover Langevin piston method and Langevin dynamics, respectively[70]. No anisotropic cell fluctuations were observed. For each system, eight replicates of 100 ns simulation were performed, and snapshots were saved at 100 ps intervals for further analysis.

The root mean square distance (RMSD) and principal component analysis (PCA) were calculated using GROMACS software[67,68]. To calculate the interaction energy between VPS26A and SNX27, the molecular mechanics with generalized Born and surface area solvation (MM/GBSA) method was used[43]. Residue decomposition analysis within the MM/GBSA framework was used to determine the contribution of each residue.

Viral propagation, quantification, and infection of SARS-CoV-2

A clinically isolated SARS-CoV-2 NCCP43344strain (Korean National Culture Collection for Pathogens Collection number: NCCP-43344) was provided by Prof. MS Park of Korea University. For the propagation of viruses, ACE2-overexpressing HeLa cells were infected by SARS-CoV-2 with 10 multiplicity of infection (MOI) and then culture supernatant was harvested 24 h post-infection. The harvested supernatant was filtered and stocked at −80 °C. For plaque formation assay, one of the stock vials was used to infect Vero cells, which were obtained from the Ministry of Food and Drug Safety (Osong, Republic of Korea). Infected cells then incubated with culture media containing 1% low gelling temperature agarose (Lonza #50101, Rockland, ME) for 48 h. Viral plaques were visualized with Neutral Red Solution (Sigma #2889, Sigma-Aldrich, St. Louis, MO) for additional 24 h and were counted to determine the plaque-forming unit of the viral stock. For viral infection assays, target cells were incubated with the virus for 1 h, after which the medium was replaced with fresh medium supplemented with 2% FBS until further experimentation.

For the quantification of the SARS-CoV-2 virus secretion, viral RNA in cell culture supernatant was extracted using a QIAamp Viral RNA Mini Kit (QIAGEN #52906, Valencia, CA), as per the manufacturer's instructions. Quantitative PCR was performed with a Luna® Universal One-Step RT-qPCR Kit (New England Biolabs Inc., Ipswich, MA, USA) using the ABI Prism 7000 detection system (Applied Biosystems, Waltham, MA, USA). For amplification, 2 µL of extracted RNA was added to a mixture of 10 µL of 2× Luna® Universal One-Step Reaction Mix, 0.4 µl of 10 µM primers, 0.2 µl of 10 µM probe and 1 µL of 20× Luna WarmStart® RT Enzyme Mix adjusted for a total reaction volume of 20 µL with RNase-free water. Amplification was carried out using the optimal thermocycling condition outlined in the manufacturer's protocol for 40 cycles. The following primer-probe sets, targeting nsp14, were used: forward primer 5′- TGGGGYTTTACRGGTAACCT-3′, reverse primer 5′- AACRCGCTTAACAAAGCACTC-3′, probe 5′-56-FAM- FAM-TAGTTGTGA/ZEN/TGCWATCATGACTAG-3IABkFQ-3′. The standard curve was generated by conducting qRT-PCR, using serially diluted virus stock. Then, Ct values were converted into viral titer (pfu/mL).

Statistical analysis
The results are presented as the mean ± standard error of the mean (SEM), using the data obtained from multiple experiments. Statistical analyses were conducted using appropriate tests, such as a two-tailed Student's *t*-test or one-way analysis of variance, followed by Tukey's multiple comparison test. GraphPad Prism 8 (GraphPad Software, Inc., La Jolla, CA, USA) was used for the statistical analysis. A *p*-value under 0.05 was considered statistically significant.

Chemicals and antibodies
Further materials and reagents used in this study are listed in Supplementary Data 6–8.

Reporting summary
Further information on research design is available in the Nature Portfolio Reporting Summary linked to this article.

Data availability
All data supporting the findings of this study are available within the main text, main figures, and Supplementary Information. The original ICC image files generated in this study have been deposited in the EBI BioImage Archive under accession code S-BIAD3018. Source data are provided with this paper.

References

1. Palade, G. Intracellular aspects of the process of protein synthesis. *Science* **189**, 347–358 (1975).
2. Rothman, J. E. Mechanisms of intracellular protein transport. *Nature* **372**, 55–63 (1994).
3. Nickel, W. & Rabouille, C. Mechanisms of regulated unconventional protein secretion. *Nat. Rev. Mol. Cell Biol.* **10**, 148–155 (2009).
4. Schotman, H., Karhinen, L. & Rabouille, C. dGRASP-mediated noncanonical integrin secretion is required for Drosophila epithelial remodeling. *Dev. Cell* **14**, 171–182 (2008).
5. Rabouille, C. Pathways of unconventional protein secretion. *Trends Cell Biol.* **27**, 230–240 (2017).
6. Filaquier, A., Marin, P., Parmentier, M. L. & Villeneuve, J. Roads and hubs of unconventional protein secretion. *Curr. Opin. Cell Biol.* **75**, 102072 (2022).
7. Rabouille, C., Malhotra, V. & Nickel, W. Diversity in unconventional protein secretion. *J. Cell Sci.* **125**, 5251–5255 (2012).
8. Riordan, J. R. et al. Identification of the cystic fibrosis gene: cloning and characterization of complementary DNA. *Science* **245**, 1066–1073 (1989).
9. Farinha, C. M. & Amaral, M. D. Most F508del-CFTR is targeted to degradation at an early folding checkpoint and independently of calnexin. *Mol. Cell Biol.* **25**, 5242–5252 (2005).
10. Ward, C. L., Omura, S. & Kopito, R. R. Degradation of CFTR by the ubiquitin-proteasome pathway. *Cell* **83**, 121–127 (1995).
11. Kopito, R. R. Biosynthesis and degradation of CFTR. *Physiol. Rev.* **79**, S167–S173 (1999).
12. Gee, H. Y., Noh, S. H., Tang, B. L., Kim, K. H. & Lee, M. G. Rescue of DeltaF508-CFTR trafficking via a GRASP-dependent unconventional secretion pathway. *Cell* **146**, 746–760 (2011).
13. Park, H., Shin, D. H., Sim, J. R., Aum, S. & Lee, M. G. IRE1α kinase-mediated unconventional protein secretion rescues misfolded CFTR and pendrin. *Sci. Adv.* **6**, eaax9914 (2020).
14. Noh, S. H. et al. Specific autophagy and ESCRT components participate in the unconventional secretion of CFTR. *Autophagy* **14**, 1761–1778 (2018).
15. Park, H. et al. TMED3 complex mediates ER stress-associated secretion of CFTR, pendrin, and SARS-CoV-2 spike. *Adv. Sci.* **9**, e2105320 (2022).
16. Watanabe, Y., Allen, J. D., Wrapp, D., McLellan, J. S. & Crispin, M. Site-specific glycan analysis of the SARS-CoV-2 spike. *Science* **369**, 330–333 (2020).
17. Cortese, M. et al. Integrative imaging reveals SARS-CoV-2-induced reshaping of subcellular morphologies. *Cell Host Microbe* **28**, 853–866.e855 (2020).
18. Zhang, J. et al. SARS-CoV-2 remodels the Golgi apparatus to facilitate viral assembly and secretion. *PLoS Pathog.* **21**, e1013295 (2025).
19. Ghosh, S. et al. β-coronaviruses use lysosomes for egress instead of the biosynthetic secretory pathway. *Cell* **183**, 1520–1535.e1514 (2020).
20. Noh, S. H., Kim, Y. J. & Lee, M. G. Autophagy-related pathways in vesicular unconventional protein secretion. *Front. Cell Dev. Biol.* **10**, 892450 (2022).
21. Villeneuve, J. et al. Unconventional secretion of FABP4 by endosomes and secretory lysosomes. *J. Cell Biol.* **217**, 649–665 (2018).
22. Seaman, M. N. J. The retromer complex: from genesis to revelations. *Trends Biochem. Sci.* **46**, 608–620 (2021).
23. Gee, H. Y., Kim, J. & Lee, M. G. Unconventional secretion of transmembrane proteins. *Semin. Cell Dev. Biol.* **83**, 59–66 (2018).
24. Liu, J. J. Retromer-mediated protein sorting and vesicular trafficking. *J. Genet Genomics* **43**, 165–177 (2016).
25. Kerr, M. C. et al. A novel mammalian retromer component, Vps26B. *Traffic* **6**, 991–1001 (2005).
26. Cullen, P. J. Endosomal sorting and signalling: an emerging role for sorting nexins. *Nat. Rev. Mol. Cell Biol.* **9**, 574–582 (2008).
27. Vagnozzi, A. N. & Praticò, D. Endosomal sorting and trafficking, the retromer complex and neurodegeneration. *Mol. Psychiatry* **24**, 857–868 (2019).
28. Hanley, S. E. & Cooper, K. F. Sorting nexins in protein homeostasis. *Cells* **10**, 17 (2020).
29. Temkin, P. et al. SNX27 mediates retromer tubule entry and endosome-to-plasma membrane trafficking of signalling receptors. *Nat. Cell Biol.* **13**, 715–721 (2011).
30. Steinberg, F. et al. A global analysis of SNX27-retromer assembly and cargo specificity reveals a function in glucose and metal ion transport. *Nat. Cell Biol.* **15**, 461–471 (2013).
31. Loo, L. S., Tang, N., Al-Haddawi, M., Dawe, G. S. & Hong, W. A role for sorting nexin 27 in AMPA receptor trafficking. *Nat. Commun.* **5**, 3176 (2014).
32. Gallon, M. et al. A unique PDZ domain and arrestin-like fold interaction reveals mechanistic details of endocytic recycling by SNX27-retromer. *Proc. Natl. Acad. Sci. USA* **111**, E3604–E3613 (2014).
33. Kim, J. Y. et al. Inhibitory regulation of cystic fibrosis transmembrane conductance regulator anion-transporting activities by Shank2. *J. Biol. Chem.* **279**, 10389–10396 (2004).
34. Lee, J. H. et al. Dynamic regulation of cystic fibrosis transmembrane conductance regulator by competitive interactions of molecular adaptors. *J. Biol. Chem.* **282**, 10414–10422 (2007).
35. Kinseth, M. A. et al. The Golgi-associated protein GRASP is required for unconventional protein secretion during development. *Cell* **130**, 524–534 (2007).
36. Kim, J. et al. Monomerization and ER relocalization of GRASP is a requisite for unconventional secretion of CFTR. *Traffic* **17**, 733–753 (2016).
37. Simonetti, B. et al. SNX27-retromer directly binds ESCPE-1 to transfer cargo proteins during endosomal recycling. *PLoS Biol.* **20**, e3001601 (2022).
38. Steinberg, F., Heesom, K. J., Bass, M. D. & Cullen, P. J. SNX17 protects integrins from degradation by sorting between lysosomal and recycling pathways. *J. Cell Biol.* **197**, 219–230 (2012).
39. Dong, R. et al. Endosome-ER contacts control actin nucleation and retromer function through VAP-dependent regulation of PI4P. *Cell* **166**, 408–423 (2016).

40. Ghai, R. et al. Structural basis for endosomal trafficking of diverse transmembrane cargos by PX-FERM proteins. *Proc. Natl. Acad. Sci. USA* **110**, E643–E652 (2013).
41. Jumper, J. et al. Highly accurate protein structure prediction with AlphaFold. *Nature* **596**, 583–589 (2021).
42. Abramson, J. et al. Accurate structure prediction of biomolecular interactions with AlphaFold 3. *Nature* **630**, 493–500 (2024).
43. Valdes-Tresanco, M. S., Valdes-Tresanco, M. E., Valiente, P. A. & Moreno, E. gmx_MMPBSA: a new tool to perform end-state free energy calculations with GROMACS. *J. Chem. Theory Comput.* **17**, 6281–6291 (2021).
44. Okiyoneda, T. et al. Peripheral protein quality control removes unfolded CFTR from the plasma membrane. *Science* **329**, 805–810 (2010).
45. Young, A. et al. Dynasore inhibits removal of wild-type and ΔF508 cystic fibrosis transmembrane conductance regulator (CFTR) from the plasma membrane. *Biochem. J.* **421**, 377–385 (2009).
46. Welz, T., Wellbourne-Wood, J. & Kerkhoff, E. Orchestration of cell surface proteins by Rab11. *Trends Cell Biol.* **24**, 407–415 (2014).
47. Ou, X. et al. Characterization of spike glycoprotein of SARS-CoV-2 on virus entry and its immune cross-reactivity with SARS-CoV. *Nat. Commun.* **11**, 1620 (2020).
48. Song, M. S. et al. Tubular ER structures shaped by ER-phagy receptors engage in stress-induced Golgi bypass. *Dev. Cell* **60**, 1568–1585.e1511 (2025).
49. Yang, B. et al. SNX27 suppresses SARS-CoV-2 infection by inhibiting viral lysosome/late endosome entry. *Proc. Natl. Acad. Sci. USA* **119**, e2117576119 (2022).
50. van Weering, J. R., Verkade, P. & Cullen, P. J. SNX-BAR proteins in phosphoinositide-mediated, tubular-based endosomal sorting. *Semin. Cell Dev. Biol.* **21**, 371–380 (2010).
51. Hayashi, H. et al. Sorting nexin 27 interacts with multidrug resistance-associated protein 4 (MRP4) and mediates internalization of MRP4. *J. Biol. Chem.* **287**, 15054–15065 (2012).
52. Cattin-Ortolá, J. et al. Sequences in the cytoplasmic tail of SARS-CoV-2 Spike facilitate expression at the cell surface and syncytia formation. *Nat. Commun.* **12**, 5333 (2021).
53. Zhao, L. et al. SARS-CoV-2 spike protein harnesses SNX27-mediated endocytic recycling pathway. *MedComm* **2**, 798–809 (2021).
54. Saraste, J., Enyioko, M., Dale, H., Prydz, K. & Machamer, C. Evidence for the role of Rab11-positive recycling endosomes as intermediates in coronavirus egress from epithelial cells. *Histochem. Cell Biol.* **158**, 241–251 (2022).
55. Rowe, R. K., Suszko, J. W. & Pekosz, A. Roles for the recycling endosome, Rab8, and Rab11 in hantavirus release from epithelial cells. *Virology* **382**, 239–249 (2008).
56. Coller, K. E. et al. Molecular determinants and dynamics of hepatitis C virus secretion. *PLoS Pathog.* **8**, e1002466 (2012).
57. Prydz, K. & Saraste, J. The life cycle and enigmatic egress of coronaviruses. *Mol. Microbiol.* **117**, 1308–1316 (2022).
58. Ribeiro, C. M. & Boucher, R. C. Role of endoplasmic reticulum stress in cystic fibrosis-related airway inflammatory responses. *Proc. Am. Thorac. Soc.* **7**, 387–394 (2010).
59. Sim, J. R. et al. Amelioration of SARS-CoV-2 infection by ANO6 phospholipid scramblase inhibition. *Cell Rep.* **40**, 111117 (2022).
60. Joung, J. et al. Genome-scale CRISPR-Cas9 knockout and transcriptional activation screening. *Nat. Protoc.* **12**, 828–863 (2017).
61. Mirdita, M. et al. ColabFold: making protein folding accessible to all. *Nat. Methods* **19**, 679–682 (2022).
62. Oh, K. S. et al. Overlooked KCNQ4 variants augment the risk of hearing loss. *Exp. Mol. Med.* **55**, 844–859 (2023).
63. Evans, R. et al. Protein complex prediction with AlphaFold-multimer. Preprint at https://www.biorxiv.org/content/10.1101/2021.10.04.463034v2 (2021).
64. Pettersen, E. F. et al. UCSF ChimeraX: structure visualization for researchers, educators, and developers. *Protein Sci.* **30**, 70–82 (2021).
65. Jo, S., Kim, T., Iyer, V. G. & Im, W. CHARMM-GUI: a web-based graphical user interface for CHARMM. *J. Comput. Chem.* **29**, 1859–1865 (2008).
66. Brooks, B. R. et al. CHARMM: the biomolecular simulation program. *J. Comput. Chem.* **30**, 1545–1614 (2009).
67. Lee, J. et al. CHARMM-GUI input generator for NAMD, GROMACS, AMBER, OpenMM, and CHARMM/OpenMM simulations using the CHARMM36 additive force field. *J. Chem. Theory Comput.* **12**, 405–413 (2016).
68. Abraham, M. J. et al. GROMACS: high performance molecular simulations through multi-level parallelism from laptops to supercomputers. *SoftwareX* **1**, 19–25 (2015).
69. Ryckaert, J.-P., Ciccotti, G. & Berendsen, H. J. Numerical integration of the cartesian equations of motion of a system with constraints: molecular dynamics of n-alkanes. *J. Comput. Phys.* **23**, 327–341 (1977).
70. Nosé, S. A unified formulation of the constant temperature molecular dynamics methods. *J. Chem. Phys.* **81**, 511–519 (1984).

Acknowledgements

The authors thank the Medical Illustration & Design team at Yonsei University College of Medicine for providing support with the medical illustrations, Benjamin J. Latimer for his editorial assistance, and the Yonsei-Carl Zeiss Advanced Imaging Center for their technical assistance. This research was supported by grants 2021R1I1A1A01049255 (to S.H.N.), 2022R1A2C3002917 (M.G.L.), RS-2022-NR067483 (M.G.L., J.M.L.), RS-2024-00351254 (H.-S.C.) and RS-2025-18362970 (M.G.L. and H.-S.C.) from the National Research Foundation (NRF) of Korea funded by the Ministry of Education and the Ministry of Science and ICT, and the grant RS-2024-00404555 (M.G.L.) and RS-2025-25422732 (M.G.L.) from the Korea Health Industry Development Institute (KHIDI) funded by the Ministry of Health & Welfare, Republic of Korea. M.G.L. was supported by the SBS Foundation.

Author contributions

Y.J.K. and C.L. conducted the molecular experiments and analyzed the data. S.K.S. performed the CRISPR-Cas9 screening. J.W.R. and D.H.S. performed PCA analysis, MD simulations, and predicted the protein structures using AlphaFold. H.R.L. carried out the immunocytochemistry experiments. S.J.H. performed experiments with authentic virus. N.C., H.S.C., and H.-S.C. conducted the SPR assays. H.K.K. and H.S.K. designed and assisted with the CRISPR-Cas9 screening experiments. H.Y.G. designed and analyzed the experiments using AlphaFold. J.M.L. designed and analyzed experiments with authentic SARS-CoV-2. M.G.L. and S.H.N. designed and analyzed all experiments and wrote the manuscript.

Competing interests

The authors declare no competing interests.

Additional information

Supplementary information The online version contains supplementary material available at https://doi.org/10.1038/s41467-026-71409-9.

Correspondence and requests for materials should be addressed to Min Goo Lee or Shin Hye Noh.

Peer review information *Nature Communications* thanks Kota Saito and the other anonymous, reviewer(s) for their contribution to the peer review of this work. A peer review file is available.